

Pierre Adrien (Orcid ID: 0000-0001-8625-9125)
Nadeau Daniel F (Orcid ID: 0000-0002-4006-2623)
Isabelle Pierre-Erik (Orcid ID: 0000-0002-2819-1377)
Ancil François (Orcid ID: 0000-0003-4568-4883)

Characteristic Time Scales of Evaporation of a Subarctic Reservoir

Adrien Pierre^{1,2}, Daniel F. Nadeau^{1,2}, Antoine Thiboult^{1,2}, Alain N. Rousseau³, Alain Tremblay⁴, Pierre-Érik Isabelle^{1,2}, François Ancil^{1,2}

¹ Department of Civil and Water Engineering, Université Laval, Québec, QC, Canada

² CentrEau – Water Research Centre, Université Laval, Québec, QC, Canada

³ Institut National de la Recherche Scientifique – Centre Eau Terre Environnement, Québec, QC, Canada

⁴ Hydro-Québec, Montréal, Québec, Canada

Corresponding Author: Adrien Pierre (adrien.pierre.1@ulaval.ca)

Abstract

Water bodies such as lakes and reservoirs affect the regional climate by acting as heat sinks and sources through the evaporation of substantial quantities of water over several months of the year. Unfortunately, energy exchange observations between deep reservoirs and the atmosphere remain rare in northeastern North America, which has one of the highest densities of water bodies in the world. This study characterizes the dynamics of turbulent heat fluxes by analysing in-situ observations of a compact and dimictic reservoir (50.69°N, 63.24°W) located in a subarctic environment. The reservoir is characterized by a mean depth of 44 m and a surface area of 85 km². Two eddy covariance (EC) systems, one on a raft and one onshore, were deployed from 2018 June 27 to 2022 June 12. The thermal regime of the reservoir was monitored using vertical chains of thermistors. Results indicate a mean annual evaporation rate of 590 ± 66 mm, which is equivalent to $\approx 51\%$ of the annual precipitation, with 84% of the evaporation occurring at a high rate from August to freeze-up in late December through episodic pulses. It was difficult to close the energy balance because of the magnitude and the large time lag of the heat storage term. To circumvent this problem, we opted to perform calculations for a year that started from the first of March, as the heat storage in the water column was at its lowest at that point and could thus be ignored. From June to December, monthly Bowen ratios increased from near-zero negative values to about 1.5. After September, due to smaller vapor pressure deficits, latent heat fluxes steadily decreased until the reservoir had a complete ice cover. Opposite diurnal cycles of sensible and latent heat fluxes were

This article has been accepted for publication and undergone full peer review but has not been through the copyediting, typesetting, pagination and proofreading process which may lead to differences between this version and the [Version of Record](#). Please cite this article as doi: [10.1002/hyp.14842](https://doi.org/10.1002/hyp.14842)

This article is protected by copyright. All rights reserved.

revealed during the open water period, with sensible heat fluxes peaking at night and latent heat fluxes peaking in the afternoon.

Keywords: Eddy-Covariance, Energy Balance, Evaporation, Subarctic reservoir, Time Scales.

Accepted Article

1. INTRODUCTION

Reservoirs are subject to significant water level fluctuations due to evaporation (latent heat flux, LE), which is not only a key component of reservoir mass and energy balances, but can affect some vital functions such as freshwater supply, irrigation, hydropower and navigation (Friedrich et al., 2018). In some arid regions of the world, structural measures are put in place to limit evaporation, such as floating balls or lattices (Assouline et al., 2021; Assouline et al., 2011). Evaporation is intangible and therefore a difficult hydrological flux to measure, making it difficult to fully understand its magnitude and controlling mechanisms.

Several studies have focused on reservoir evaporation, but few in cold regions. Therefore, there is a need for additional in situ observations to further improve our understanding of the processes involved and document their characteristic time scales. Tanny et al. (2008) reported an average evaporation rate of 5.5 mm day^{-1} from July to September in the small Eshkol reservoir in Israel (33°N), which has a hot and arid climate. Further north, in the shallow Eastmain-1 reservoir in Canada (52°N), Strachan et al. (2016) found the evaporation rate to be 3.1 mm day^{-1} between August and October. These studies indicate that even in cold regions, reservoir evaporation can be substantial. Additional studies over reservoirs are nevertheless necessary to improve the parameterization of water-atmosphere exchanges (Mackay et al., 2017).

In cold climates, dimictic reservoirs undergo two turnover periods per year. Their thermal regime typically evolves into three successive phases (Cole et al., 2016). During the ice cover phase, ice acts as a lid over the water body, preventing direct interactions between the atmosphere and the water column. Latent heat fluxes tend to remain low during this period (Wang et al., 2016). After the ice break-up period, the spring turnover takes place, resulting in an overall vertical mixing of the entire column. The heat storage period then starts and lasts until the end of summer. Latent heat fluxes remain low during this phase, with frequent stable atmospheric stratification. The third and final phase corresponds to the heat release period. This is characterized by a decline in water temperature due to a substantial release of energy into the atmosphere through turbulent heat fluxes that are high and sustained day and night (Blanken et al., 2011).

While evaporation varies seasonally in response to the three thermal phases, it also fluctuates on smaller time scales in response to meteorological forcing. For instance, incoming shortwave radiation causes latent heat fluxes to peak during the day (Lensky et al., 2018). The atmospheric demand for water vapour, driven by wind speed and vapour pressure deficit, is also known to modulate evaporation in water bodies (Pérez et al., 2020). Evaporative demand can vary within

a single day. For instance, changing wind direction can lead to a reduced or enhanced sheltering effect, increasing or decreasing evaporation rates (Markfort et al., 2010; Venäläinen et al., 1998). Evaporation can also vary over the course of a few days, due to passing synoptic systems that can generate sustained evaporation (Laird et al., 2002; Spence et al., 2013). Blanken et al. (2000) found that 50% of annual evaporation over the Great Slave Lake occurred over only 25% of the year through episodic evaporation water losses. Moreover, thermocline depth and intensity, which depend in part on the reservoir morphometry (Gorham, 1964), influence turbulent heat fluxes by limiting or enhancing the energy available in the upper water layers. Indeed, Piccolroaz et al. (2015) identified a positive feedback between the lake surface temperature and the stratification dynamics of Lake Superior, Canada. The timing of evaporation occurs at different scales and remains poorly documented or correlated with physical drivers (Beck et al., 2018) for deep reservoirs in the boreal zone of northeastern Canada.

Northeastern America is one of the densest regions of lakes and reservoirs around the world (Downing et al., 2006). These lakes and reservoirs are considered to be climate sentinels (Adrian et al., 2009; Williamson et al., 2009a) as well as integrators and regulators of climate change (Williamson et al., 2009b). Wang et al. (2018) showed that modifications in surface energy allocation under warmer climate conditions will accelerate global lake evaporation. Moreover, in-situ evaporation observations are needed to develop and improve lake models (Kallel, 2023; McJannet et al., 2017) for future climate estimates, particularly in remote areas. There is a lack of direct in-situ measurements of turbulent heat fluxes over reservoirs in remote northern regions. The central goal of this study is to characterize the temporal dynamics of turbulent heat fluxes over a compact (i.e. a low surface to volume ratio), dimictic and hydropower reservoir located in a subarctic environment. To achieve this goal, two flux towers, one mounted on a floating raft deployed during the ice-free period and one on a nearby shoreline, were deployed to measure surface fluxes using the eddy covariance method from June 2018 to June 2022. The specific objectives were to quantify turbulent heat fluxes at daily, monthly, and annual time scales, and to identify the key processes and surface energy budget terms that govern LE at each time scale. The paper is organized as follows. We first introduce the study site and measurement methods. Then, we describe the meteorological conditions over the whole study period and the driving factors of turbulent heat fluxes for each time scale. Finally, uncertainties underlying the flux calculations are discussed, including a description of the closure of the energy balance.

2. MATERIALS AND METHODS

2.1 Study Site

The study site is located at the southern tip of the Romaine-2 hydropower reservoir (50.68°N, 63.25°W; Fig. 1a), 80 km north of the city of Havre-Saint-Pierre, which is on the North Shore of the Gulf of St. Lawrence, Quebec, Canada. The Romaine-2 reservoir is a dimictic water body that is ice-free from May to December. The regional climate has a mean annual air temperature and precipitation of 1°C and 1167 mm, respectively. Precipitation was estimated using our measurements and Environment Canada data recorded near our study site. This is typical of the subarctic (Dfc) Köppen-Geiger climate classification type (Beck et al., 2018). The reservoir, which flooded in 2014, drains a 14,351-km² area that is mostly covered with a spruce-moss forest. At its southern end, the reservoir is about 1 km-wide, and sits at an elevation of 244 m above mean sea level. When full, it has a surface area of 85.6 km² and a maximum depth of 101 m (mean depth of 44 m). It has an elongated north-south shape and steep banks channelling the near-surface winds. The study period extended from 27 June 2018 to 12 June 2022.

Figure 1: (a) Location of the Romaine-2 reservoir in North America (red square). (b) Satellite image (Sentinel-2A, 2022-01-26) of the Romaine-2 reservoir in winter. The black rectangle indicates the area of the experimental setup (c). (c) Elevation map indicating precisely where the spillway, intake, flux towers and thermistor chains (indicated by TC) are located. The red contour lines represent the flux footprints areas (90% and 80% for the raft and for the shore station respectively, refer to Sec. 2.2).

2.2 Raft and Shore Flux Towers

Figure 2 shows the two flux towers that were deployed on the research site: a 3 × 3-m raft (measurement height of 2.0 m) deployed from June to October each year and a permanent shore tower (measurement height fluctuating between 11 and 28 m depending on the water level) (Fournier et al., 2021; Pierre et al., 2022). At both sites, the eddy covariance technique was used to calculate 30-min averaged turbulent heat fluxes from raw 10-Hz turbulence data.

The raft was anchored between two islands to offer protection against large waves, in a 30-m deep section of the reservoir. The raft hosted a fast-response sonic anemometer coupled with an infrared gas analyzer (IRGASON, Campbell Scientific, USA), a net radiometer (Kipp & Zonen, The Netherlands) and a temperature probe (HMP45C, Campbell Scientific, USA), all mounted 2 m above the water surface. Turbulence sensors were oriented eastward to capture the prevailing wind directions while minimizing flow distortion by the mast. The raft slowly oscillated due to wave-induced motions. To decontaminate raw wind measurements, an

accelerometer (AHRS, Lord Sensing MicroStrain, USA) was attached adjacent to the anemometer to record pitch, yaw, and roll angles at a frequency of 10 Hz.

At the shore site, the flux tower was equipped with a combined sonic anemometer and infrared gas analyzer (IRGASON, Campbell Scientific, USA), installed 11 m above the maximum water level and pointing toward the reservoir in the NNW direction. A complete meteorological setup was also deployed: a temperature probe (HMP45C, Campbell Scientific, USA), a TB4 tipping bucket (Hyquest Solutions, USA) for rainfall measurement, a propeller anemometer (05103, R.M.Young, USA), and a four-component net radiometer (CNR4, Kipp & Zonen, The Netherlands). The last two instruments were installed at heights of 10.3 m and 12.3 m, respectively. The radiometer measured all terms of the radiation budget, namely incoming and outgoing shortwave and longwave radiation, but since the instrument was installed on the shore, it did not report the radiation emitted/reflected by the reservoir.

Flux footprints were calculated for both eddy-covariance set-up following Kljun et al. (2015). Both flux towers displayed a local flux footprint, i.e. an area of a few hectares (Fig. 1c). Moreover, the footprint of the raft always remained above the water surface, no matter what the wind direction and water level of the reservoir were. On the other hand, the footprint of the flux tower installed on the shore encompassed the water and the land surfaces depending on the wind direction and the reservoir water level. However, only data with wind direction from the reservoir were considered (Sec. 2.3). Therefore, the results reported in this study represent turbulent heat fluxes from the reservoir only.

The atmospheric variables (wind speed, air temperature, vapor pressure deficit, etc.) measured at the raft and at the shore station were merged into a single dataset as follows: the raft data were kept when available, otherwise the shore data were retained.

Figure 2: The two eddy covariance measurement setups deployed on and around the Romaine-2 reservoir. Raft station (left, photo taken looking west) and shore station (right, photo taken looking north) with the following instruments: (a) net radiometer, (b) air temperature probe, (c) accelerometer, (d) sonic anemometer and infrared gas analyzer, and (e) propeller anemometer. Photos were provided by Hydro-Québec and taken on 2019 June 13, at approximately 2 m below the maximum reservoir level.

A complete year-long net radiation time series was created using the following strategy. We used the net radiation that was measured on the raft when it was deployed (June–October). When ice was present on the reservoir, it was typically covered in snow. We therefore assumed that the emitted/reflected radiation measured at the shore station during that time was equivalent to what would have been measured on the reservoir. During the transition periods, we estimated the reflected radiation on the reservoir with a simple albedo formula based on that by Patel et al. (2019). The longwave radiation emitted during the transition periods was estimated from the Stefan–Boltzmann law. This was done by taking an emissivity of 0.995 and

extrapolating the water temperature profile in the top meter of water to estimate the water skin temperature for periods when no direct measurements were available.

2.3 Turbulent Heat Fluxes

Sensible (H) and latent heat fluxes (LE) (both in W m^{-2}) were calculated using the covariance between the vertical wind speed w (m s^{-1}) and air temperature T (K), as well as between w and the specific humidity q (kg kg^{-1}), such that:

$$H = \rho_a c_{pa} \overline{w' T'} \quad (1)$$

$$LE = L_v \rho_a \overline{w' q'} \quad (2)$$

where ρ_a is the dry air density (kg m^{-3}), c_{pa} is the specific heat of humid air ($\text{J kg}^{-1} \text{K}^{-1}$) and L_v is the latent heat of vaporization (J kg^{-1}). Here, primes denote fluctuations from the 30-min average, indicated by an overbar.

Raw wind velocity data from the raft were first corrected for wave-induced motion, using the accelerometer data, following the method proposed by Miller et al. (2008). In short, the apparent wind measured by the sonic anemometer was corrected to account for Euler angles, angular velocities and linear accelerations monitored by the accelerometer. Then, for the shore and raft flux towers, we processed the turbulence data using the EddyPro® software, version 7.0 (LI-COR Biosciences, USA). In doing so, we applied time-lag compensation, linear detrending, double rotation approach (Baldocchi et al., 1988; Wilczak et al., 2001), density fluctuation compensation (Webb et al., 1980), spike removal (Papale et al., 2006), and other statistical tests (Vickers et al., 1997). Poor-quality data were flagged (Mauder et al., 2011) and removed. Data from the raft and shore stations were aggregated into one dataset by favoring data with the best quality criteria (Mauder et al., 2013). Note that shore data were retained only when winds originated from the reservoir. To complete the final dataset, gap-filling was implemented based on the method developed by Reichstein et al. (2005).

Over the whole study period (1447 days), 57 % of the turbulent flux data had to be gap-filled since the raft was only deployed from June to October and the shore flux tower was frequently exposed to winds from the surrounding land. We assessed flux errors by applying the Finkelstein et al. (2001) random uncertainty method.

2.4 Water Temperature and Transparency

The vertical water temperature profile was continuously measured with two chains of temperature probes (HOBO TidBit UTBI-001, Onset, USA) that were designed with a higher

resolution near the surface and a coarser resolution deeper in the water (Fig. 3). These are referred to as thermistor chains (TCs). The first measurement site, TC₁, consisted of a 15-m chain deployed in a 30-m deep section of the reservoir, in the vicinity of the raft. The second measurement site, TC₂, consisted of a 70-m chain located in a 100-m deep section of the reservoir, 1 km south of the raft. At both sites, skin temperatures were obtained using floating sensors sheltered from incoming solar radiation by a white piece of foam. The chains were designed to withstand variations in water levels by using additional rope. A pressure sensor (HOBO water level logger u20-001-03, Onset, USA) was added to each chain to correct for the effects of rope tilt on the exact vertical position of the probes.

Water transparency was also periodically measured using a Secchi disc. The mean Secchi depth (*SD*) was 4 ± 0.04 m. Following Koenings et al. (1991), we then assumed that the mean product of $SD \times K_d$ was 2.28, thus we estimated the vertical attenuation coefficient K_d to be 0.57 m^{-1} for water of moderate transparency. Consequently, 50% of the incident energy flux density is absorbed in the first 1.2 m of water and 99% over the first 8.1 m of water.

Figure 3: (a) Schematic of the thermistor chain (TC) components, (b) TidBit temperature probes (HOBO TidBit UTBO-001, Onset, USA) installed on the chains, and (c) the resolution of temperature measurements presented on a logarithmic scale (in m).

2.5 Energy Balance Ratio

The energy balance ratio (Feng et al., 2016) allows us to quantify the energy balance closure and therefore to correct underestimated turbulent heat fluxes (see Sect. 3.3). It is defined as follows:

$$EBR = \frac{H+LE}{R_n-\Delta H_S} \times 100 \quad (3)$$

where R_n is the net radiation and ΔH_S is the heat storage variation along the water column, defined as

$$\Delta H_S = \int_0^h \rho_w c_{pw} \frac{\overline{\Delta T_w}}{\Delta t} dh \quad (4)$$

where ρ_w is the water density (kg m^{-3}), c_{pw} is the specific heat of water ($\text{J kg}^{-1} \text{K}^{-1}$), ΔT_w is the water temperature difference between two timesteps (K), Δt is the period (30 min), and h is the water layer thickness (m). To determine the EBR, ΔH_S was calculated over the entire depth of the epilimnion, which is the distance between the surface (0 m) and the position of the thermocline (h). Note that the epilimnion thickness varies over the year. On average, $h = 15$ m from June to October, $h = 30$ m from November to December, and $h = 0$ m from January to

May. Note that we did not consider the energy used to melt the snow in the EBR. Indeed, no measurements of the snow cover temperature were made. Although this term appeared only in April and May, it may explain the non-closure of the annual energy budget.

Moreover, it is well known that eddy covariance data underestimate turbulent heat fluxes (Foken, 2008). We implemented an alternative approach to adjust the turbulent heat fluxes according to the annual EBR ratio: the corrected turbulent heat fluxes were obtained by redistributing the missing energy over a so-called ‘energy year’, namely from March 1 to February 28/29 of the next year. Since energy storage is typically at its minimum value at this time of the year, this allowed us to discard that term and write $R_n = H + LE$. By doing so, Equation 3 becomes

$$EBR = \frac{H+LE}{R_n} \times 100 \quad (5)$$

2.6 Ice Cover

Ice cover was monitored using a time-lapse camera (Reconyx, Holmen, WI, USA) that took hourly photos of the southern edge of the reservoir. Water temperatures were also used to identify the solar radiation penetration into the water column and ice formation, as ice and snow cover reduce or prevent radiation from entering the water column. More precisely, the completion of freezing takes place when the water surface is completely covered with ice. The end of the ice-cover period occurs when the reservoir becomes completely free of ice. In both cases, the identification of the dates was done by inspecting hourly pictures of the water surface of the southern end of the reservoir and the time series of the temperature sensors at 0.2 m depth.

Figure 4 illustrates the key phases of the reservoir regime. The ice-free period (Fig. 4a) and the ice-cover period (Fig. 4c) are separated by the onset (Fig. 4b) and break-up (Fig. 4d) of ice.

Figure 4: Photographs (looking north) illustrating some key phases of the reservoir regime: (a) open-water period (12 September 2018), (b) start of freeze-up (23 December 2018), (c) full ice and snow cover (7 February 2019), and (d) ice breakup (23 May 2019).

3. RESULTS & DISCUSSION

3.1 Meteorological Conditions

The meteorological conditions at Romaine-2 reservoir are relevant to understand the context of the climatic conditions that underlie the measured turbulent flux processes. For instance, the

air temperature is linked to the sensible heat flux, and the vapour vapor pressure deficit (*VPD*) drives the magnitude of the latent heat flux. The overall meteorological conditions observed over the Romaine-2 reservoir were typical of a subarctic climate (Fig. 5), with cool and humid summers along with cold winters. Wind speed (*WS*) was generally quite high, particularly in the fall and winter when daily averages occasionally reached 15 m s^{-1} , but showed a marked decline in summer. The reservoir was mostly colder than the air above it between May and July (the heat storage period). The vapour pressure deficit (*VPD*) values were high from May to September with a mean value of 581 Pa, and low from October to April with a mean value of 276 Pa.

The duration of the ice cover period varied between 130 and 160 days, with an average of 150 days. The onset of the ice cover period occurred when the reservoir was fully covered with ice, and the end was defined when the ice and snow cover had fully disappeared from the surface. The onset and the end of the freeze-up period showed an interannual variability of 15 days on average: the start and the end occurred on average on January 1 and May 16, respectively. In addition, ice cores were extracted in the vicinity of the shore flux tower in 2020 and showed ice thicknesses of 50 cm, 75 cm and 85 cm mid-February, end of March and mid-April, respectively. Regarding the snow cover, depths of 20 cm, 13 cm and 6 cm were recorded during these sampling campaigns, respectively.

Figure 5: Daily means of (a) 2-m air (T_a) and near-surface water temperatures (T_w), (b) vapor pressure deficit (*VPD*), and (c) wind speeds (*WS*) collected at the raft and shore sites. The period with ice cover (shaded area) was determined from time-lapse photos.

The distribution of the wind direction measured from the raft and shore flux towers followed a bimodal pattern. Prevailing winds were from the NNE and SSW during the study period. The 30-min mean wind speed was 5.6 m s^{-1} while the maximum wind speed reached 19.4 m s^{-1} .

3.2 Heat Fluxes

3.2.1 Daily Scale

Figure 6 illustrates the average diurnal cycles of H and LE during ice cover (January to mid-May), the heat storage phase (mid-May to August), and heat release (September to December). The last two phases are defined based on the heat storage presented (refer to Sec. 3.2.2).

During the ice cover periods, LE remained low ($< 20 \text{ W m}^{-2}$) and positive, which is indicative of sublimation, while H was negative ($< -10 \text{ W m}^{-2}$). Both turbulent heat fluxes had diurnal cycles with an amplitude lower than 10 W m^{-2} . The corresponding Bowen ratios $\beta (= H/LE)$ were small and negative when LE was between 5 W m^{-2} and 10 W m^{-2} . These results were expected, as ice and snow covered the water surface from early January until mid-May, suggesting high albedo and preventing the surface from heating up enough to produce stronger turbulent heat fluxes.

From mid-May to August, LE values remained low, with an average of nearly 30 W m^{-2} and a maximum of up to 60 W m^{-2} at 14:00 LT (local time). H then showed a clear diurnal cycle, at -30 W m^{-2} at 15:00 LT and close to 0 W m^{-2} at night. Values of -60 W m^{-2} were reached in early afternoon. Similarly, the mean Bowen ratio exhibited a daily cycle with a minimum value of -0.7 in the afternoon and a maximum value of 0.1 at night, for a total amplitude of 0.8 .

During the heat release phase (September to December), LE always remained larger than H , meaning that energy was mainly released through phase change (evaporation). One striking feature is that LE and H had opposite daily patterns: (i) LE reached a maximum at around 15:00 LT while H reached a minimum, and (ii) LE reached a minimum at 00:00 LT while H peaked at 05:00 LT. LE peaked in the afternoon when the incident solar radiation reached its maximum value, warming up the water surface during the day. Maximum H values occurred at night when the maximum water–air temperature difference was observed. At a similar temporal scale, Nordbo et al. (2011) observed fluxes over the small, boreal Lake Valkea-Kotinen in Finland and showed that the highest values of LE and H occurred in June, peaking at 15:00 LT and at 06:00 LT respectively. Therefore, in the present study, the Bowen ratio exhibited an explicit diurnal cycle: the highest values were around 0.95 at night because of high H and low LE values and the lowest values were around 0.40 in the day because of low H and high LE values. As a result, heat was released by two different mechanisms depending on the time of the day: through both turbulent heat fluxes at night and mainly through evaporation during the day. Overall, the sensible heat fluxes H contributes to the heat stored by the water body early in summer that will be released as latent and sensible heat fluxes in fall.

Figure 6: Average diurnal cycle of (top) latent heat flux, (middle) sensible heat flux, and (bottom) Bowen ratios, with the interquartile (dark shading) and the 10 to 90 quantile zones (light shading). The left column are data for January to mid-May (ice cover), the central column covers mid-May to August (heat storage), and the right column covers September to December (heat release). Note that the range of the ordinate values varies from one plot to the other. All times are local.

Condensation episodes ($LE < 0 \text{ W m}^{-2}$) occurred occasionally throughout the study period. During winters, small and short condensation episodes occurred almost every day. However, during the vernal turnover, conditions became very stable, and the atmosphere was much warmer than the water surface, which was nearly constant at 4°C . Consequently, only a few condensation events were recorded between May 1 and July 17, with cumulative amounts of 2.2 mm, 0.6 mm and 3.4 mm in 2019, 2020 and 2021, respectively. Figure 7 presents examples of condensation events that occurred in June, temporarily reaching -10 W m^{-2} or 0.35 mm day^{-1} . Although condensation was highest in June, it remained low compared to evaporation, which easily exceeded 100 W m^{-2} throughout the September-December period.

Figure 7: Daily mean latent heat flux for 2019 (light blue), 2020 (purple) and 2021 (blue), illustrating the occurrence of condensation episodes between June 13 and 30.

The reservoir was exposed to many episodes of sustained evaporation, defined as consecutive 24-h periods with a daily mean $LE \geq 100 \text{ W m}^{-2}$ (i.e., daily mean $LE \geq 3.5 \text{ mm}$), ranging from one to several days. Of those, the most modest episode caused 3.5 mm of evaporation in one day, while the largest episode caused 29.3 mm of evaporation in 6 days ($\approx 5 \text{ mm day}^{-1}$). Figure 8 presents the number of sustained evaporation events for each month and their durations. 80% of sustained evaporation events lasted only 2 days or less. On average, there were 6 and 3.7 occurrences of 1-day and 2-day events, respectively, and less than one 3-day event per year. The number of occurrences of sustained evaporation events varied from year to year, but overall, between 8 and 14 for the study period. The mean rate of evaporation was 0.2 mm h^{-1} for all events. As a comparison, Blanken et al. (2011) reported that most of the evaporation from Lake Superior occurred in 2.5- to 3-day episodic pulses.

Figure 8: Sustained evaporation events, defined as consecutive days with at least 3.5 mm of daily evaporation. (a) Number of occurrences per month: A (August), S (September), O (October), N (November), D (December); and (b) number of occurrences for different durations. Note that the points above and below the curve represent the maximum and minimum number of occurrences, while the continuous line links the average of each month.

Figure 9 presents several variable time series during three strong evaporative events. These episodes occur when air becomes drier (decline of at least 50% of the specific humidity) in conjunction with high wind speeds. These situations seem to be the successful combination to enable high evaporation rate. Correlation coefficients between latent heat flux and wind speed were 0.36, 0.7 and 0.74 for the 2018/09/04, 2018/09/06-10, and 2020/08/14-15 events,

respectively. Moreover, high evaporation took place with an increase in vapour pressure deficit from 400 Pa to 1000 Pa on average. However, no correlation was found between latent heat flux and vapour pressure deficit.

Moreover, during these three evaporation events, the winds were from the SSW, indicating that they were channelled into the main axis of the reservoir. In addition, during these evaporation events, the air was drier than usual with a specific humidity below 5.5 g kg^{-1} , which was within the 30th quantile over the months of August and September. These episodes were each time due to the occurrence of a high-pressure system in conjunction with the passage of a cold front. The anticyclones brought drier air masses from the north and prevailing clear-sky conditions promoted incoming solar radiation on the water surface, while cold fronts generated strong winds after their transit. The combined effect of these phenomena enhanced the evaporative process.

Figure 9: Three sustained evaporation episodes (grey shaded areas; left, 1-day and 5-day episodes in September 2018, and right, 2-day episode in August 2020) with 30-min time series of (a, b) latent heat fluxes, (c, d) specific humidity, (e, f) wind speed, (g, h) atmospheric pressure, and (i, j) vapor pressure deficit. Shaded zones indicate high evaporation events.

3.2.2 Monthly Scale

Figure 10 displays monthly averaged turbulent heat fluxes, net radiation and heat storage over the whole study period. Latent heat fluxes remained positive. LE began to rise in July when stratification of the reservoir settled in, and then sharply increased in August. It peaked in September at 78 W m^{-2} when the cumulative heat storage reached its maximum (refer to Fig. 10) and remained greater than 60 W m^{-2} all the way to December. 84% of the annual total evaporation took place in the last five months of the year. However, in our study, LE decreased gradually due to the declining vapour pressure deficit that followed the decline in air temperature. In winter and spring, LE stayed below 20 W m^{-2} and reached its minimum in June, during the ice-free period (Fig. 5).

Sensible heat fluxes were negative from February to July, with values less than -10 W m^{-2} and reaching as low as -20 W m^{-2} when the reservoir was colder than the air. On average, values remained positive from August to January. In June, the reservoir was ice-free while the water column was under vernal transition, with upper layers that were not warm enough to stratify (i.e., below 3.98°C , the temperature of maximum water density). The water surface temperature stayed far below the air temperature, preventing H from becoming positive and enabling LE to become negative. In summer and fall, the surface layers were warmer than the air above the

water. H increased steadily until December, reaching 80 W m^{-2} , and then decreased abruptly in January as the water surface froze.

Figure 10: (a) Monthly average sensible heat flux (red), latent heat flux (blue), net radiation (black) and 70-m deep heat storage (orange) from June 2018 to December 2021. Bars indicate monthly minimum and maximum average values. (b) Monthly Bowen ratio. The error bars indicate the maximum and minimum values observed for each month.

From May to August, net radiation (R_n) was high, contributing mostly to the storage of heat in the reservoir (ΔH_s), while turbulent heat fluxes were relatively low. Nearly all the energy brought in by R_n was used to increase the heat storage term. During the fall and early winter, R_n declined rapidly while LE and H increased, fuelled by the energy stored in the reservoir, firmly establishing the heat release period of the reservoir. We observed a three-month delay between the maximum summer net radiation in June and the maximum latent heat flux in September. The delay was six months between that peak of net radiation and the maximum sensible heat flux in December. We also observed different delays between the maximum surface water temperature and the maximum LE and H , which were delayed by one and four months, respectively.

Heat storage started in May and ended in early September (a 3.5-month period): the heat content of the water body rose by 130 W m^{-2} , 220 W m^{-2} and 175 W m^{-2} over the months of May, June and July, respectively. Heat release followed and lasted about 4 months until ice-on. The heat release rate was lower from September to October (-73 W m^{-2}) compared to November to December (-250 W m^{-2}). Overall, heat storage exhibited larger day-to-day fluctuations than heat release.

The Bowen ratios exhibited high negative values during the first seven months of each year due to low LE values. During the last month of the storage period (August, Fig. 10), it stayed around zero in August before gradually increasing to about 1.5 in December. This indicates that the reservoir was mostly releasing heat through sensible heat flux. Before freeze-up, evaporation was constrained by the small vapour pressure deficit induced by the negative air temperatures. For this reason, the sensible heat flux became the preferred means of heat transfer to the atmosphere in November and December. Then, when freeze-up occurred at the beginning of January, both turbulent heat fluxes were limited by the formation of a thin ice layer. Moreover, at this time of the year, the reservoir heat content was much lower than that during the autumn turnover, and water surface temperatures remained close to zero, reducing the potential turbulent heat fluxes to the atmosphere.

The energy state of the reservoir is closely tied to the stability regime of the overlying atmosphere. During heat release (September to end of December), the overlying atmosphere was unstable, while it remained mostly stable during the heat storage (mid-May to August) and ice-cover periods. Figure 11 explores the relationship between daily LE and atmospheric stability ζ ($\zeta = z/L_{ob}$, where L_{ob} is the Obukhov length) for heat storage and release. It confirms that larger daily evaporation occurs under near-neutral ($\zeta \approx 0$) and unstable conditions ($\zeta < 0$), and that stable conditions ($\zeta > 0$) are related to low evaporation rates. Note that condensation occurred primarily under near-neutral and stable conditions. This is consistent with the findings from Blanken et al. (2011) for Lake Superior, where 89% of the annual evaporation occurred when there was unstable atmospheric stratification. It is also consistent with the Rouse et al. (2003) study at Great Slave Lake, where 85% to 90% of evaporation occurred during a period when the atmosphere was unstable.

Figure 11: Daily latent heat flux as a function of atmospheric stability ($\zeta = z/L_{ob}$ where z is the measured height and L_{ob} refers to the Obukhov length) for the ice-free periods (May 15 to December 31) from 2018 to 2021.

When looking at the monthly layer energy balance of the reservoir using equation 3, we noted that there was a significant non-closure (see Sec. 3.3). This is due to the time scale difference between the heat storage in the water column and the remaining terms (turbulent heat fluxes and net radiation). Indeed, due to the high thermal inertia and the high specific heat of water, the net radiation that was received in summer accumulated in the water column and was only released in autumn. This feature makes it difficult to calculate the EBR on a monthly scale. Within this context, correcting turbulent heat fluxes to account for the energy imbalance (Foken, 2008) using the monthly EBR is problematic unless accurate measurements of lateral energy inputs are available. This challenge is developed in section 3.3 with monthly EBR from 2019 to 2021.

3.2.3 Annual Scale

Calculating annual reservoir evaporation values is challenging. The underestimation of turbulent heat fluxes by the eddy-covariance technic implies that the observed annual values must be corrected using the EBR over an ‘energy year’ (see Sec. 2.5). Since $R_n > H + LE$, the missing energy can then be redistributed by preserving the observed Bowen ratio, as discussed

in Mauder et al. (2018). By doing so, the EBR (Equation 5) was 80%, 69%, and 76% for the years 2019–20, 2020–21, and 2021–22, respectively.

Figure 12 illustrates the yearly cumulative evaporation for three energy years, from 2019 to 2022. The mean annual non-corrected evaporation was 442 mm and did not vary much from year to year, with a minimum of 423 mm and a maximum of 456 mm. When correcting for the energy imbalance using the annual EBR values, the annual evaporation values reached 555 mm, 656 mm and 559 mm for 2019–20, 2020–21 and 2021–22, respectively (refer to Table 1). Note that the inter-annual variabilities of cumulative evaporation were 7.2% and 18% for non-corrected and corrected values, respectively. In fact, 50% of the total measured evaporation occurred over 24%, 27% and 26% of the days for 2019–20, 2020–21 and 2021–22, respectively. This is consistent with Blanken et al. (2000), who found a mean value of 22.5% for the Great Slave Lake.

Figure 12: Cumulative annual evaporation from 1 March to 28/29 February of the following year, for 2019–20, 2020–21 and 2021–22. Pale green, red, blue and grey bars represent the duration of the respective ice cover periods. Horizontal bars at the end of the energy period represent corrected annual evaporation, compensating for the lack of closure of the energy balance based on the annual EBR (see Table 1).

Few studies have focused on annual scales of lake or reservoir evaporation in the boreal biome. In Canada, Strachan et al. (2016) reported that the evaporation rate at the Eastmain-1 reservoir was 595 mm yr^{-1} , reaching $100 \text{ mm month}^{-1}$ in summer and 3.1 mm day^{-1} from August to October. Rouse et al. (2003) found the annual evaporation at Great Slave Lake to be between 384 mm and 506 mm yr^{-1} . For Lake Tännaren in Sweden, Heikinheimo et al. (1999) reported 281 mm of evaporation from May to October. Finally, Blanken et al. (2011) found the annual evaporation at Lake Superior to be up to 645 mm . However, it is important to note that these studies were all based on eddy-covariance measurements and did not take into consideration the non-closure of the energy balance, meaning that they did not correct for cumulative evaporation values. This appears to be one major shortcoming in the annual estimation of turbulent heat fluxes.

Table 1 presents important meteorological characteristics for each year of the study period. Note that 2020 experienced the lowest turbine volume in the study, probably due to the upstream flooding of the Romaine-4 reservoir, which might explain the slightly higher evaporation. The highest temperature anomaly by a fair margin occurred in 2021, while wind speed anomalies remained low and constant throughout the study period.

Table 1: Annual characteristics from 2018 to 2021. Non-corrected and corrected total of evaporation, ice cover period, turbine outflow volume, temperature and wind speed anomalies compared to 1991–2020 (ERA5 values) and total net radiation.

Years	2018 - 19	2019 - 20	2020 - 21	2021 - 22
Non-corrected total evaporation (mm)	-	446	456	423
Corrected annual evaporation (mm) see Sect. 3.3	-	555	656	559
Ice cover period (days)	-	145	133	119
Turbine outflow volume (km ³)	6.1	7.4	5.6	8.5
Temperature anomaly (°C)	-0.4	-0.4	+0.7	+3.5
Wind speed anomaly (m s ⁻¹)	+0.01	+0.2	+0.03	+0.03
Total net radiation (MJ m ⁻²)	-	1844	2046	1970

When examining the inter-annual variation of cumulative evaporation, we noted that the seasonal onset and the break-up of ice cover did not have a large impact on total yearly evaporative losses. The longer ice cover period in 2019 (145 days) than that of 2020 (133 days) resulted in lower cumulative evaporation. This trend is not repeated in 2021, which featured the shortest ice cover period (119 days) and lower cumulative evaporation compared to 2020 (Fig. 12). We also noted that the timing of ice onset was very consistent, as it began around January 1 of each year, while ice break-up was more variable between years. As for duration, the onset of ice lasted between two and three weeks while ice break-up lasted five to seven weeks prior to the reservoir becoming completely ice-free.

3.3 Uncertainties

There are uncertainties that affected the EC measurements that were used in this study. Random sampling uncertainties were calculated following Finkelstein et al. (2001) and amounted to $\approx 2\%$ for both sensible and latent heat fluxes over the whole study period. In addition, the error associated with gap-filling was noteworthy for H , LE and R_n because of the difficulty of measuring fluxes over an inland water body. The use of a raft results in oscillations that must be considered in the calculation process, while the use of a flux tower on the shore limits the measurement period over the reservoir.

EC measurements were also subject to underestimations linked to the lack of energy balance closure (Foken, 2008), which is best described in terms of the energy balance ratio (EBR, equation 3). Figure 13 illustrates the monthly EBR values in the reservoir for 2019 to 2021. This confirms that the energy budget layer was subject to non-closure. The large overestimation of the January EBR is due to the very small denominator during this period. Indeed, both net radiation and heat storage are negative and close together at this time of year, allowing the January EBR to reach very high values (~ 150).

Figure 13: Monthly EBR from March 2019 to December 2021. Note that ΔH_S were calculated over a 15-m depth except for November and December 2020 and 2021, for which it was calculated for an h of 30-m and 44-m depths respectively.

Some uncertainties lie in the evaluation of ΔH_S . The monthly EBR was calculated using a ΔH_S for depths of 0–15 m, 0–30 m or 0–44 m, which correspond to the average depths of the thermocline for January to October, November, and December, respectively. The heat content of water layers between the surface and these depths represent good approximations of the heat storage within the water column. This is because the thermal mixing is spatially constrained by the thermocline. However, there is uncertainty in estimating these thermocline depths, which may lead to errors in the evaluation of ΔH_S .

Note that for 2019, there were no data for depths below 15 m. When we calculated ΔH_S for a 30-m and a 44-m depth, the EBR for November and December 2020 was 101% and 138% respectively. This was less than the 150% and 440% calculated for the water between the surface and 15-m depth.

4. CONCLUSION

This study quantified the temporal dynamics of evaporation over a deep, boreal, dimictic hydroelectric reservoir using two eddy-covariance setups, one mounted on a raft and one onshore. Data were collected for four years, from June 2018 to June 2022, in order to examine the daily, monthly and annual patterns of the turbulent heat fluxes.

Turbulent heat fluxes revealed opposite diurnal cycles of H and LE during heat storage and heat release periods, and the absence of a diurnal pattern during the rest of the year. LE reached its maximum at 15:00 when H reached its minimum, and LE was minimal at night at 00:00 while H peaked at 05:00 in the morning. Our monthly analysis showed that most of the latent and sensible heat fluxes occurred from August to December. Evaporation during that period accounted for 84% of total annual evaporation. Three- and six-month delays occurred between maximum summer net radiation and maximum values of LE and H , respectively, suggesting the impact of the heat storage release. Moreover, one- and four-month delays were observed between the maximum surface water temperature and maximum LE and H , respectively.

Results showed an annual evaporation of $590 \pm 66 \text{ mm yr}^{-1}$ that was quite constant from year to year, with frequent 1-day to 2-day sustained events. Latent heat flux increased earlier than the sensible heat flux but also decreased before the sensible heat flux, resulting in a Bowen ratio that varied from a near-zero negative value in July to 1.5 in December. Vapour pressure-

controlled evaporation induced a steady decline from September to December due to decreasing air temperature.

The large time lag and the magnitude of the energy storage within the water column made it difficult to close the energy balance. Therefore, in this study, we have taken that issue into account by correcting the annual cumulative evaporation while preserving the measured Bowen ratio.

Moreover, monthly, and seasonal patterns of evaporation can be related to the energy state of the reservoir. Indeed, depending on the time of year, the reservoir was either under ice cover or in heat storage or heat release conditions, which drives the magnitude of evaporation. Finally, because evaporation is likely to increase in the region due to climate change, the assessment of this energy and the associated hydraulic components remains topical and essential to understanding future trends.

ACKNOWLEDGEMENTS

The authors would like to acknowledge Hydro-Québec for their collaboration, and more specifically François Bilodeau. They are also grateful to Catherine Aubry who provide valuable insight and to Annie-Claude Parent, Dany Crépault, Denis Jobin, Doris Domart, Benjamin Bouchard, and Gonzalo Leonardini Quelca for their help in field-related activities. This research was funded by the Natural Sciences and Engineering Research Council of Canada (NSERC) through grant RDCPJ508080-16 titled, “Observation and modelling of net evaporation from a boreal hydroelectric complex (water footprint)”.

DATA AVAILABILITY: Data available upon request.

REFERENCES

- Adrian, R., O'Reilly, C. M., Zagarese, H., Baines, S. B., Hessen, D. O., Keller, W., Livingstone, D. M., Sommaruga, R., Straile, D., Van Donk, E., Weyhenmeyer, G. A., & Winder, M. (2009). Lakes as sentinels of climate change. *Limnology and Oceanography*, 54(6part2), 2283-2297. doi:https://doi.org/10.4319/lo.2009.54.6_part_2.2283
- Assouline, S., & Narkis, K. (2021). Reducing evaporation from water reservoirs using floating lattice structures. *Water Resources Research*, 57(6). doi:<https://doi.org/10.1029/2021WR029670>
- Assouline, S., Narkis, K., & Or, D. (2011). Evaporation suppression from water reservoirs: Efficiency considerations of partial covers. *Water Resources Research*, 47(7). doi:<https://doi.org/10.1029/2010WR009889>

- Baldocchi, D. D., Hincks, B. B., & Meyers, T. P. (1988). Measuring biosphere-atmosphere exchanges of biologically related gases with micrometeorological methods. *Ecology*, 69(5), 1331-1340. doi:<https://doi.org/10.2307/1941631>
- Beck, H. E., Zimmermann, N. E., McVicar, T. R., Vergopolan, N., Berg, A., & Wood, E. F. (2018). Present and future Köppen-Geiger climate classification maps at 1-km resolution. *Scientific Data*, 5(1), 180214. doi:<https://doi.org/10.1038/sdata.2018.214>
- Blanken, P. D., Rouse, W. R., Culf, A. D., Spence, C., Boudreau, L. D., Jasper, J. N., Kochtubajda, B., Schertzer, W. M., Marsh, P., & Verseghy, D. (2000). Eddy covariance measurements of evaporation from Great Slave Lake, Northwest Territories, Canada. *Water Resources Research*, 36(4), 1069-1077. doi:<https://doi.org/10.1029/1999WR900338>
- Blanken, P. D., Spence, C., Hedstrom, N., & Lenters, J. D. (2011). Evaporation from Lake Superior: 1. Physical controls and processes. *Journal of Great Lakes Research*, 37(4), 707-716. doi:<https://doi.org/10.1016/j.jglr.2011.08.009>
- Cole, G. A., & Weihe, P. E. (2016). *Textbook of limnology* (5th ed.). Prospect Heights, Ill.: Waveland Press.
- Downing, J. A., Prairie, Y. T., Cole, J. J., Duarte, C. M., Tranvik, L. J., Striegl, R. G., McDowell, W. H., Kortelainen, P., Caraco, N. F., Melack, J. M., & Middelburg, J. J. (2006). The global abundance and size distribution of lakes, ponds, and impoundments. *Limnology and Oceanography*, 51(5), 2388-2397. doi:<https://doi.org/10.4319/lo.2006.51.5.2388>
- Feng, J. W., Liu, H. Z., Sun, J. H., & Wang, L. (2016). The surface energy budget and interannual variation of the annual total evaporation over a highland lake in Southwest China. *Theoretical and Applied Climatology*, 126(1-2), 303-312. doi:<https://doi.org/10.1007/s00704-015-1585-9>
- Finkelstein, P. L., & Sims, P. F. (2001). Sampling error in eddy correlation flux measurements. *Journal of Geophysical Research: Atmospheres*, 106(D4), 3503-3509. doi:<https://doi.org/10.1029/2000JD900731>
- Foken, T. (2008). The energy balance closure problem: An overview. *Ecological Applications*, 18(6), 1351-1367. doi:<http://doi.org/10.1890/06-0922.1>
- Fournier, J., Thibault, A., Nadeau, D. F., Vercauteren, N., Anctil, F., Parent, A.-C., Strachan, I. B., & Tremblay, A. (2021). Evaporation from boreal reservoirs: A comparison between eddy covariance observations and estimates relying on limited data. *Hydrological Processes*, 35(8), e14335. doi:<https://doi.org/10.1002/hyp.14335>
- Friedrich, K., Grossman, R. L., Huntington, J., Blanken, P. D., Lenters, J., Holman, K. D., Gochis, D., Livneh, B., Prairie, J., Skeie, E., Healey, N. C., Dahm, K., Pearson, C., Finnessey, T., Hook, S. J., & Kowalski, T. (2018). Reservoir evaporation in the Western United States. *Bulletin of the American Meteorological Society*, 99(1), 167-187. doi:<http://doi.org/10.1175/BAMS-D-15-00224.1>
- Gorham, E. (1964). Morphometric control of annual heat budgets in temperate lakes. *Limnology and Oceanography*, 9(4), 525-529. doi:<https://doi.org/10.4319/lo.1964.9.4.0525>
- Heikinheimo, M., Kangas, M., Tourula, T., Venäläinen, A., & Tattari, S. (1999). Momentum and heat fluxes over lakes Tämna and Råksjö determined by the bulk-aerodynamic and eddy-correlation methods. *Agricultural and Forest Meteorology*, 98-99, 521-534. doi:[https://doi.org/10.1016/S0168-1923\(99\)00121-5](https://doi.org/10.1016/S0168-1923(99)00121-5)
- Kallel, H. (2023). Observation and modeling of heat and water exchanges between the atmosphere and an 85-km² dimictic boreal reservoir. *Journal of Hydrometeorology*.

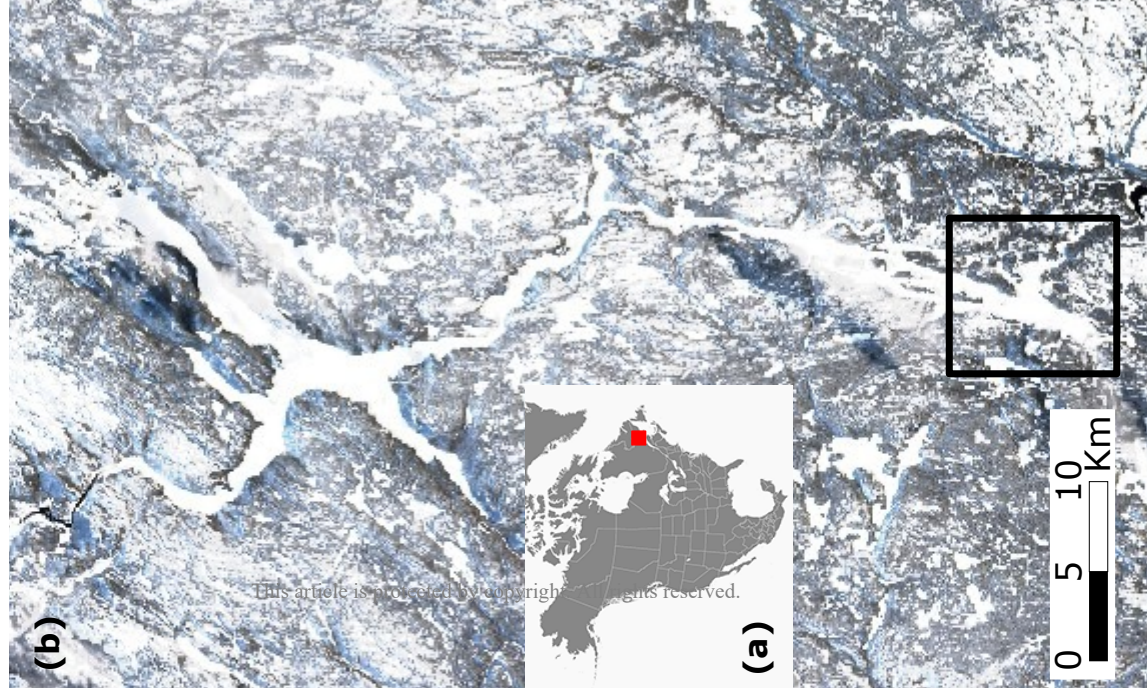
- Kljun, N., Calanca, P., Rotach, M., & Schmid, H. (2015). A simple two-dimensional parameterisation for Flux Footprint Prediction (FFP). *Geoscientific Model Development*, 8(11), 3695-3713. doi:<https://doi.org/10.5194/gmd-8-3695-2015>
- Koenings, J. P., & Edmundson, J. A. (1991). Secchi disk and photometer estimates of light regimes in Alaskan lakes: Effects of yellow color and turbidity. *Limnology and Oceanography*, 36(1), 91-105. doi:<https://doi.org/10.4319/lo.1991.36.1.0091>
- Laird, N. F., & Kristovich, D. A. R. (2002). Variations of sensible and latent heat fluxes from a great lakes buoy and associated synoptic weather patterns. *Journal of Hydrometeorology*, 3(1), 3-12. doi:[https://doi.org/10.1175/1525-7541\(2002\)003%3C0003:VOSALH%3E2.0.CO;2](https://doi.org/10.1175/1525-7541(2002)003%3C0003:VOSALH%3E2.0.CO;2)
- Lensky, N. G., Lensky, I. M., Peretz, A., Gertman, I., Tanny, J., & Assouline, S. (2018). Diurnal course of evaporation from the dead sea in summer: A distinct double peak induced by solar radiation and night sea breeze. *Water Resources Research*, 54(1), 150-160. doi:<https://doi.org/10.1002/2017WR021536>
- Mackay, M. D., Verseghy, D. L., Fortin, V., & Rennie, M. D. (2017). Wintertime Simulations of a Boreal Lake with the Canadian Small Lake Model. *Journal of Hydrometeorology*, 18(8), 2143-2160. doi:10.1175/JHM-D-16-0268.1
- Markfort, C. D., Perez, A. L. S., Thill, J. W., Jaster, D. A., Porte-Agel, F., & Stefan, H. G. (2010). Wind sheltering of a lake by a tree canopy or bluff topography. *Water Resources Research*, 46(3). doi:<https://doi.org/10.1029/2009WR007759>
- Mauder, M., Cuntz, M., Drüe, C., Graf, A., Rebmann, C., Schmid, H. P., Schmidt, M., & Steinbrecher, R. (2013). A strategy for quality and uncertainty assessment of long-term eddy-covariance measurements. *Agricultural and Forest Meteorology*, 169, 122-135. doi:<http://doi.org/10.1016/j.agrformet.2012.09.006>
- Mauder, M., & Foken, T. (2011). *Documentation and instruction manual of the Eddy-Covariance Software package TK3* (Vol. 46). Bayreuth: Arbeitsergebnisse Universität Bayreuth, Abteilung Mikrometeorologie.
- Mauder, M., Genzel, S., Fu, J., Kiese, R., Soltani, M., Steinbrecher, R., Zeeman, M., Banerjee, T., De Roo, F., & Kunstmann, H. (2018). Evaluation of energy balance closure adjustment methods by independent evapotranspiration estimates from lysimeters and hydrological simulations. *Hydrological Processes*, 32(1), 39-50. doi:<http://doi.org/10.1002/hyp.11397>
- McJannet, D., Hawdon, A., Van Niel, T., Boadle, D., Baker, B., Trefry, M., & Rea, I. (2017). Measurements of evaporation from a mine void lake and testing of modelling approaches. *Journal of Hydrology*, 555, 631-647. doi:<https://doi.org/10.1016/j.jhydrol.2017.10.064>
- Miller, S. D., Hristov, T., Edson, J., & Friehe, C. (2008). Platform motion effects on measurements of turbulence and air-sea exchange over the open ocean. *Journal of Atmospheric and Oceanic Technology*, 25(9), 1683-1694. doi:<https://doi.org/10.1175/2008JTECHO547.1>
- Nordbo, A., Launiainen, S., Mammarella, I., Lepparanta, M., Huotari, J., Ojala, A., & Vesala, T. (2011). Long-term energy flux measurements and energy balance over a small boreal lake using eddy covariance technique. *Journal of Geophysical Research - Part D - Atmospheres*, 116(D2), D02119 (02117 pp.). doi:<https://doi.org/10.1029/2010JD014542>
- Papale, D., Reichstein, M., Aubinet, M., Canfora, E., Bernhofer, C., Kutsch, W., Longdoz, B., Rambal, S., Valentini, R., Vesala, T., & Yakir, D. (2006). Towards a standardized processing of Net Ecosystem Exchange measured with eddy covariance technique: algorithms and uncertainty estimation. *Biogeosciences*, 3(4), 571-583. doi:<https://doi.org/10.5194/bg-3-571-2006>

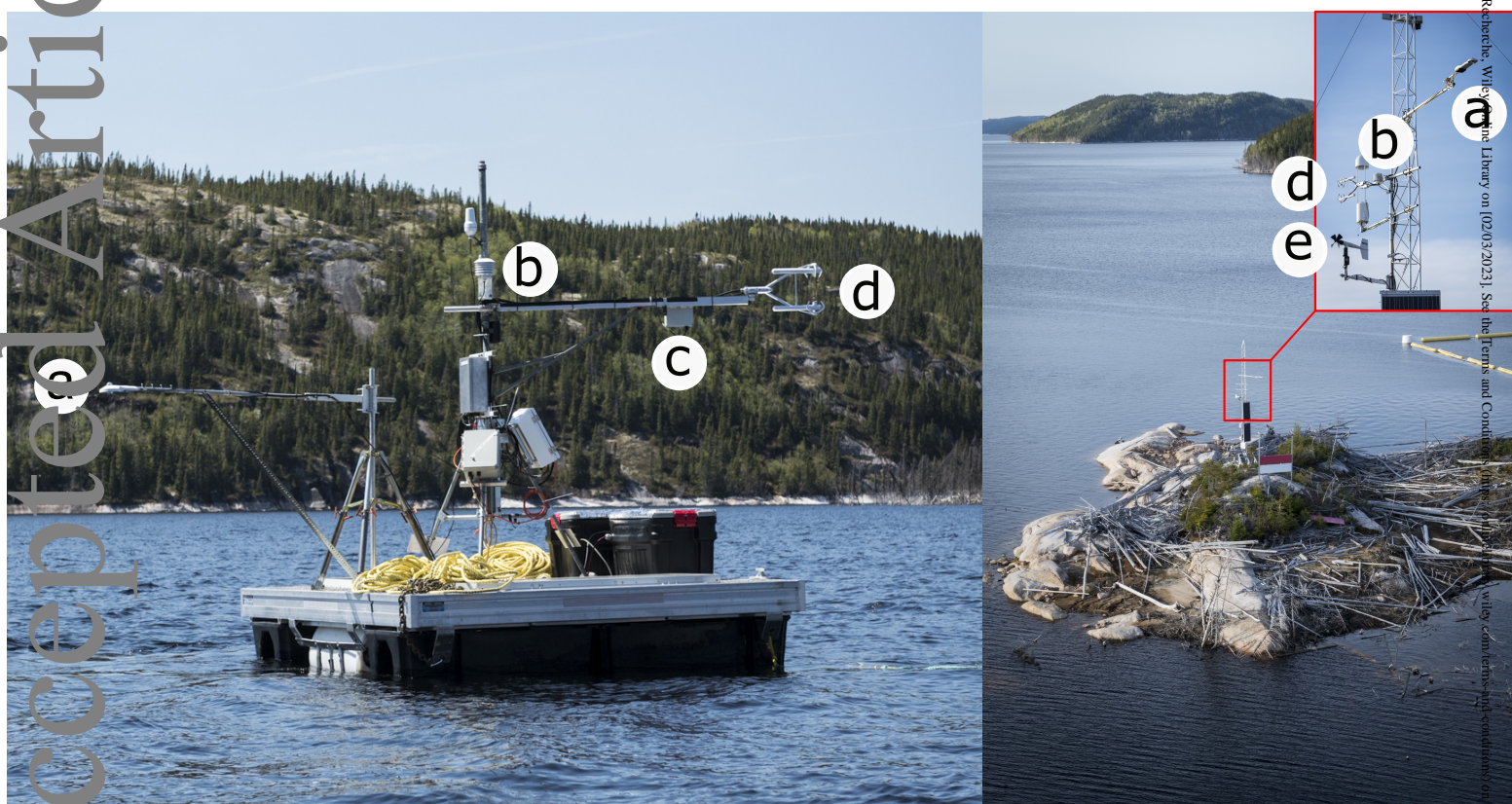
- Patel, S., & Rix, A. (2019). *Water surface albedo modelling for floating PV plants*. Paper presented at the 6th Southern African Solar Energy Conference (SASEC), Port Alfred, South Africa.
- Pérez, A., Lagos, O., Lillo-Saavedra, M., Souto, C., Paredes, J., & Arumí, J. L. (2020). Mountain lake evaporation: A comparative study between hourly estimations models and in situ measurements. *Water*, *12*(9), 2648. doi:<https://doi.org/doi:10.3390/w12092648>
- Piccolroaz, S., Toffolon, M., & Majone, B. (2015). The role of stratification on lakes' thermal response: The case of Lake Superior. *Water Resources Research*, *51*(10), 7878-7894. doi:<https://doi.org/10.1002/2014WR016555>
- Pierre, A., Isabelle, P.-E., Nadeau, D. F., Thiboult, A., Perelet, A. O., Rousseau, A. N., Anctil, F., & Deschamps, J. (2022). Estimating sensible and latent heat fluxes over an inland water body using optical and microwave scintillometers. *Boundary-Layer Meteorology*, *185*, 277-308. doi:<https://doi.org/10.1007/s10546-022-00732-7>
- Reichstein, M., Falge, E., Baldocchi, D., Papale, D., Aubinet, M., Berbigier, P., Bernhofer, C., Buchmann, N., Gilmanov, T., Granier, A., Grünwald, T., Havránková, K., Ilvesniemi, H., Janous, D., Knohl, A., Laurila, T., Lohila, A., Loustau, D., Matteucci, G., Meyers, T., Miglietta, F., Ourcival, J.-M., Pumpanen, J., Rambal, S., Rotenberg, E., Sanz, M., Tenhunen, J., Seufert, G., Vaccari, F., Vesala, T., Yakir, D., & Valentini, R. (2005). On the separation of net ecosystem exchange into assimilation and ecosystem respiration: review and improved algorithm. *Global Change Biology*, *11*(9), 1424-1439. doi:<https://doi.org/10.1111/j.1365-2486.2005.001002.x>
- Rouse, W. R., Oswald, C. M., Binyamin, J., Blanken, P. D., Schertzer, W. M., & Spence, C. (2003). Interannual and seasonal variability of the surface energy balance and temperature of central Great Slave Lake. *Journal of Hydrometeorology*, *4*(4), 720-730.
- Spence, C., Blanken, P. D., Lenters, J. D., & Hedstrom, N. (2013). The importance of spring and autumn atmospheric conditions for the evaporation regime of lake superior. *Journal of Hydrometeorology*, *14*(5), 1647-1658. doi:<https://doi.org/10.1175/JHM-D-12-0170.1>
- Strachan, I. B., Tremblay, A., Pelletier, L., Tardif, S., Turpin, C., & Nugent, K. A. (2016). Does the creation of a boreal hydroelectric reservoir result in a net change in evaporation? *Journal of Hydrology*, *540*, 886-899. doi:<https://doi.org/10.1016/j.jhydrol.2016.06.067>
- Tanny, J., Cohen, S., Assouline, S., Lange, F., Grava, A., Berger, D., Teltch, B., & Parlange, M. B. (2008). Evaporation from a small water reservoir: Direct measurements and estimates. *Journal of Hydrology*, *351*(1-2), 218-229. doi:<https://doi.org/10.1016/j.jhydrol.2007.12.012>
- Venäläinen, A., Heikinheimo, M., & Tourula, T. (1998). Latent heat flux from small sheltered lakes. *Boundary-Layer Meteorology*, *86*(3), 355-377. doi:<https://doi.org/10.1023/A:1000664615657>
- Vickers, D., & Mahrt, L. (1997). Quality control and flux sampling problems for tower and aircraft data. *Journal of Atmospheric and Oceanic Technology*, *14*(3), 512-526.
- Wang, W., Lee, X., Xiao, W., Liu, S., Wang, Y., Zhang, M., Zhao, L., & Schultz, N. (2018). Global lake evaporation accelerated by changes in surface energy allocation in a warmer climate. *Nature Geoscience*, *11*(6), 410-414. doi:<https://doi.org/10.1038/s41561-018-0114-8>
- Wang, W., Roulet, N. T., Strachan, I. B., & Tremblay, A. (2016). Modeling surface energy fluxes and thermal dynamics of a seasonally ice-covered hydroelectric reservoir. *Science of the Total Environment*, *550*, 793-805. doi:<https://doi.org/10.1016/j.scitotenv.2016.01.101>

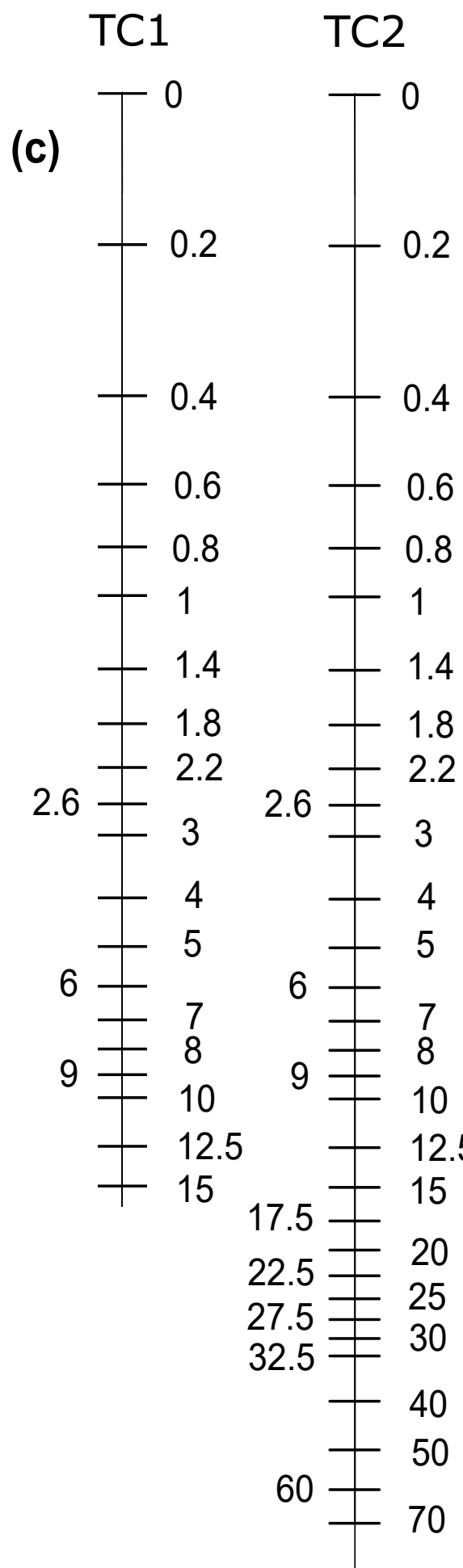
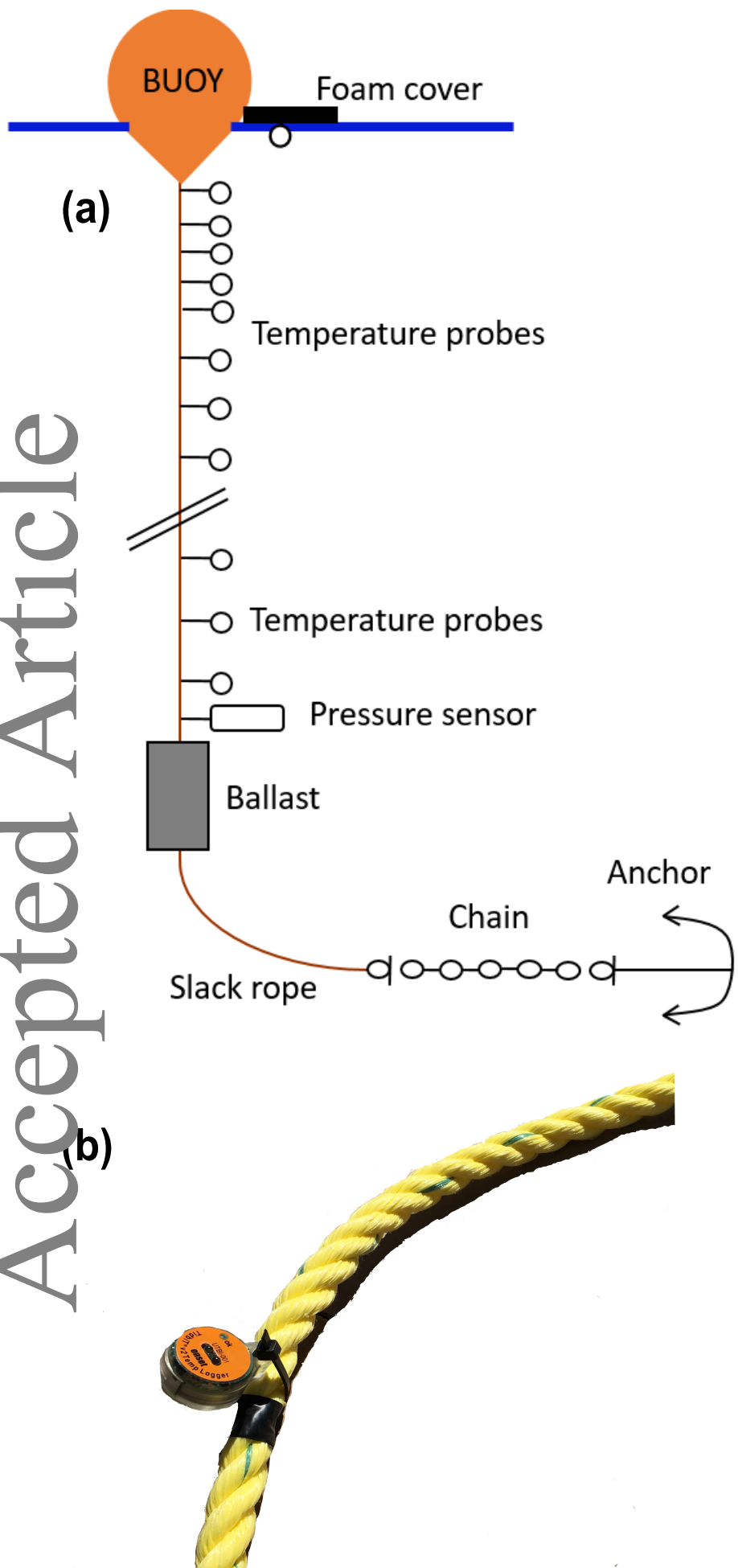
- Webb, E. K., Pearman, G. I., & Leuning, R. (1980). Correction of flux measurements for density effects due to heat and water vapour transfer. *Quarterly Journal of the Royal Meteorological Society*, 106(447), 85-100. doi:<https://doi.org/10.1002/qj.49710644707>
- Wilczak, J. M., Oncley, S. P., & Stage, S. A. (2001). Sonic anemometer tilt correction algorithms. *Boundary-Layer Meteorology*, 99(1), 127-150. doi:<https://doi.org/10.1023/A:1018966204465>
- Williamson, C. E., Saros, J. E., & Schindler, D. W. (2009a). Climate change: Sentinels of change. *Science*, 323(5916), 887-888. doi:<https://doi.org/10.1126/science.1169443>
- Williamson, C. E., Saros, J. E., Vincent, W. F., & Smol, J. P. (2009b). Lakes and reservoirs as sentinels, integrators, and regulators of climate change. *Limnology and Oceanography*, 54(6part2), 2273-2282. doi:https://doi.org/10.4319/lo.2009.54.6_part_2.2273

Table 1: Annual characteristics from 2018 to 2021. Non-corrected and corrected total of evaporation, ice cover period, turbine outflow volume, temperature and wind speed anomalies compared to 1991–2020 (ERA5 values) and total net radiation.

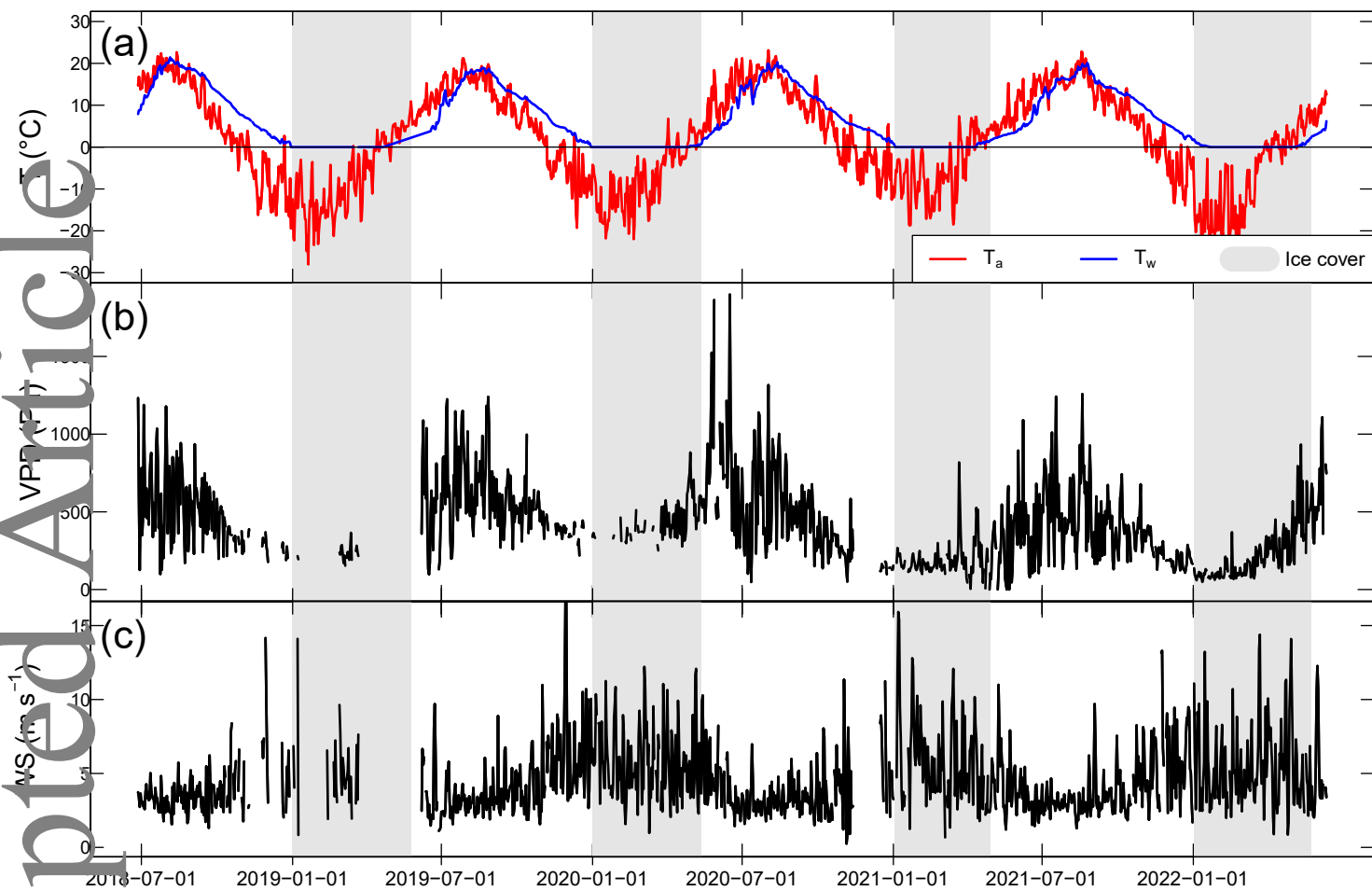
Years	2018 - 19	2019 - 20	2020 - 21	2021 - 22
Non-corrected total evaporation (mm)	-	446	456	423
Corrected annual evaporation (mm) see Sect. 3.3	-	555	656	559
Ice cover period (days)	-	145	133	119
Turbine outflow volume (km ³)	6.1	7.4	5.6	8.5
Temperature anomaly (°C)	-0.4	-0.4	+0.7	+3.5
Wind speed anomaly (m s ⁻¹)	+0.01	+0.2	+0.03	+0.03
Total net radiation (MJ m ⁻²)	-	1844	2046	1970

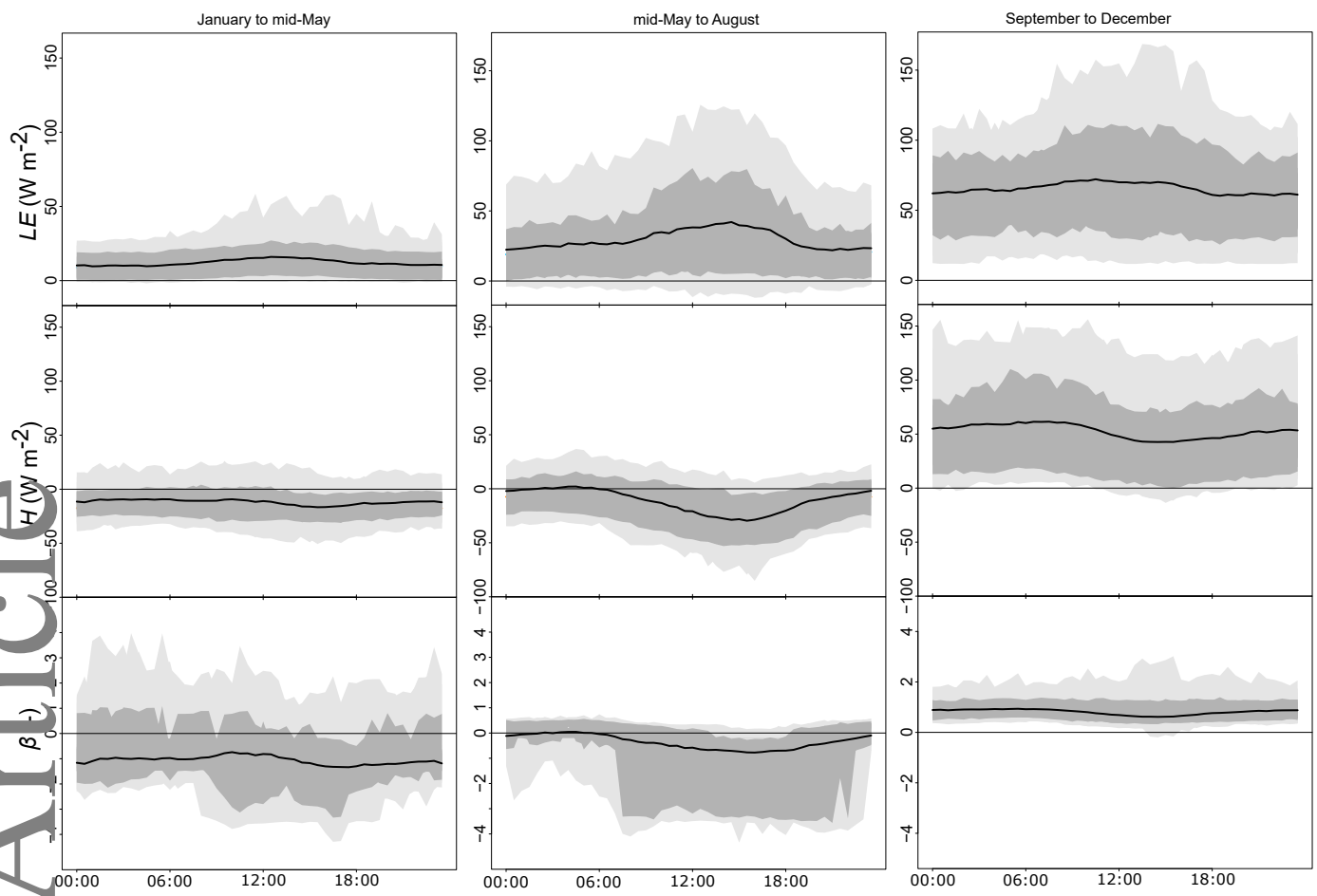




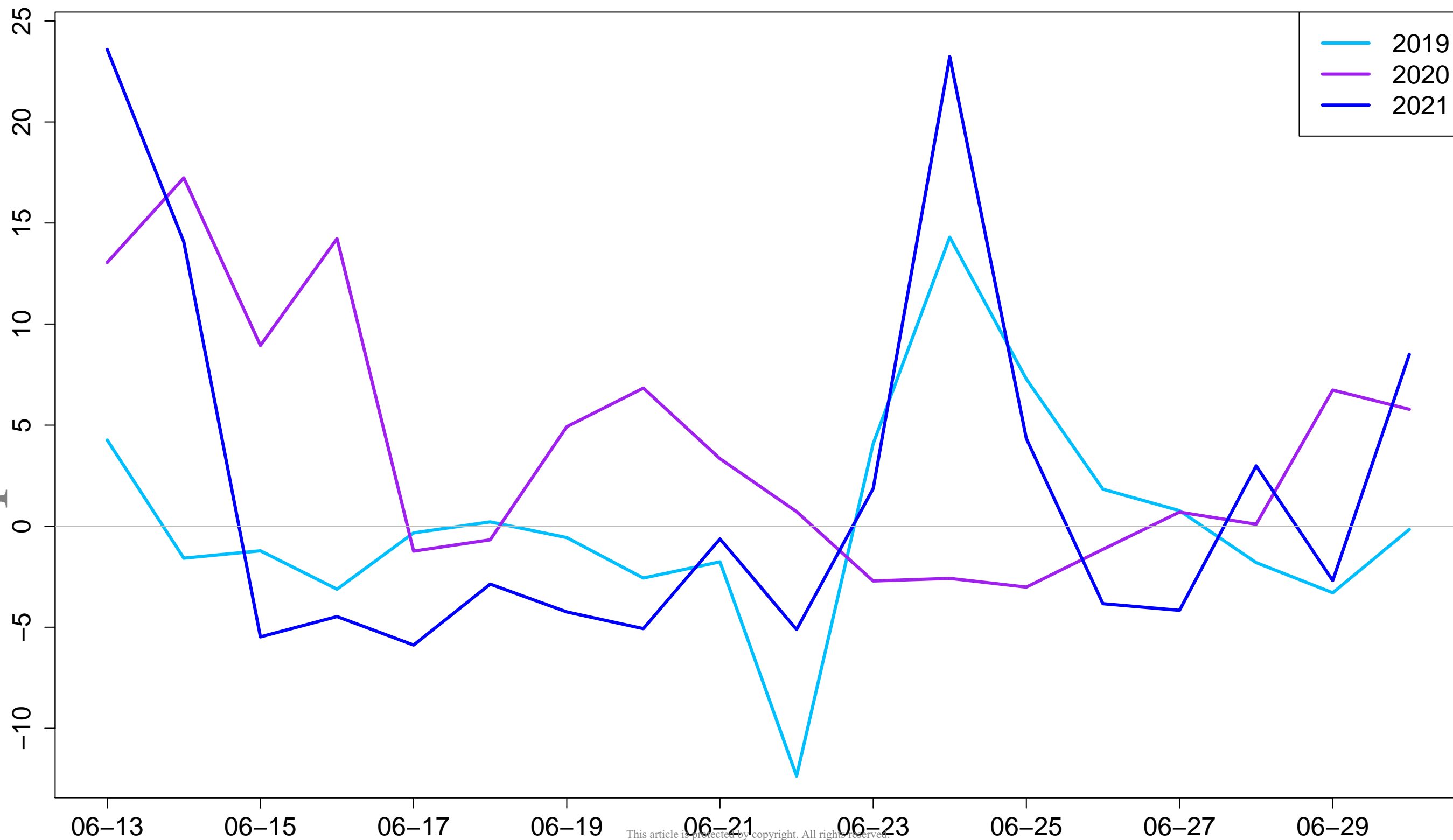




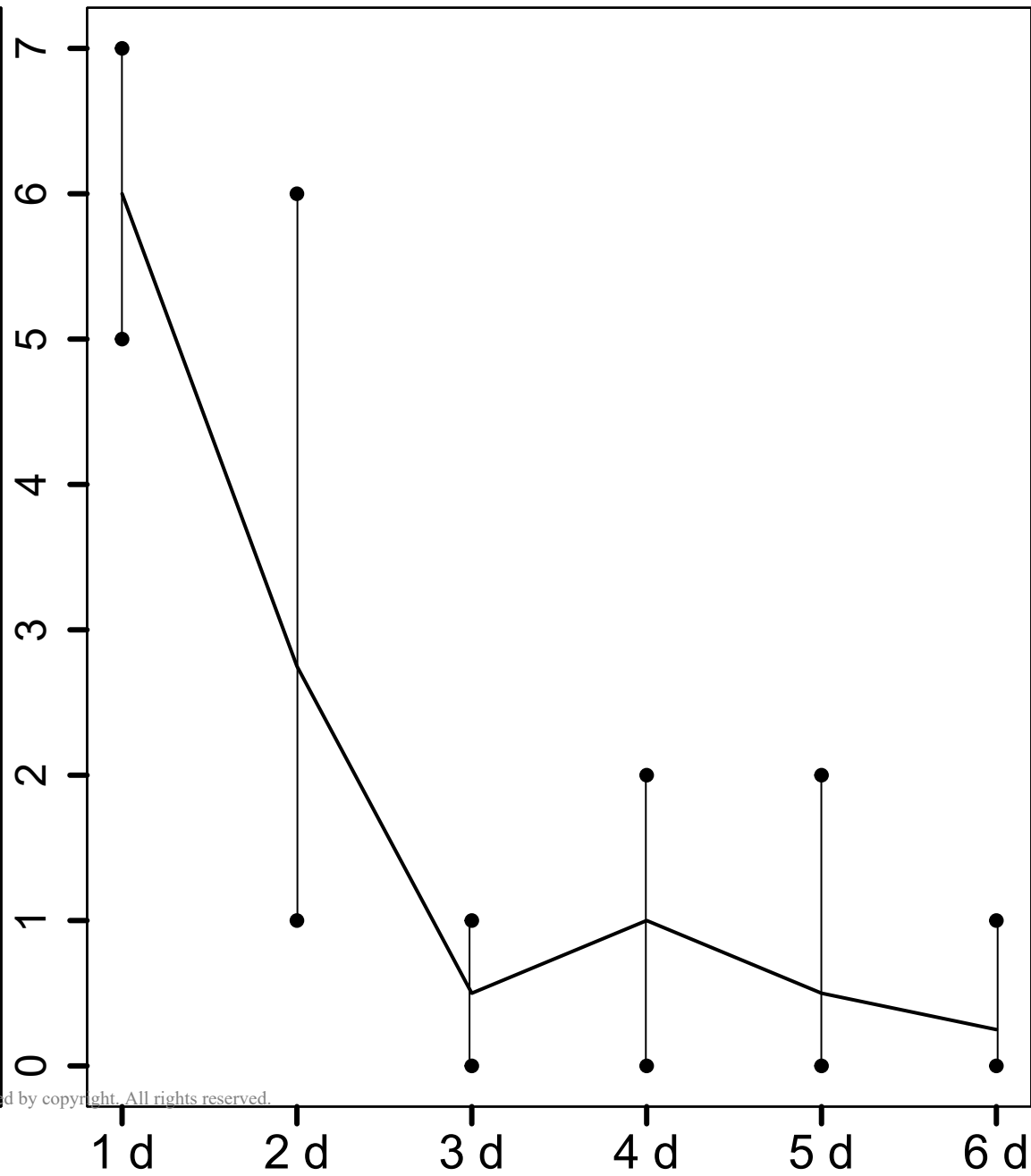
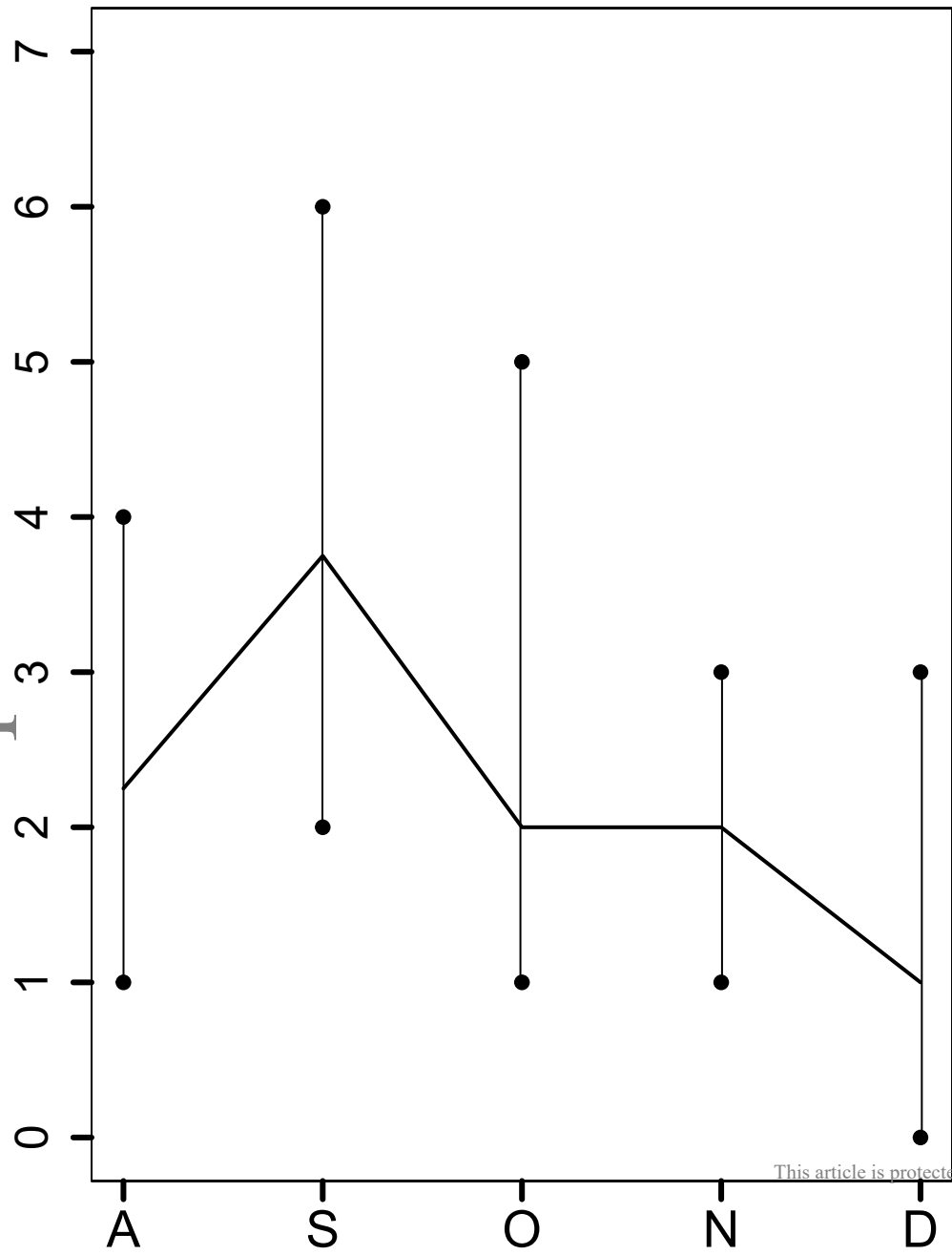




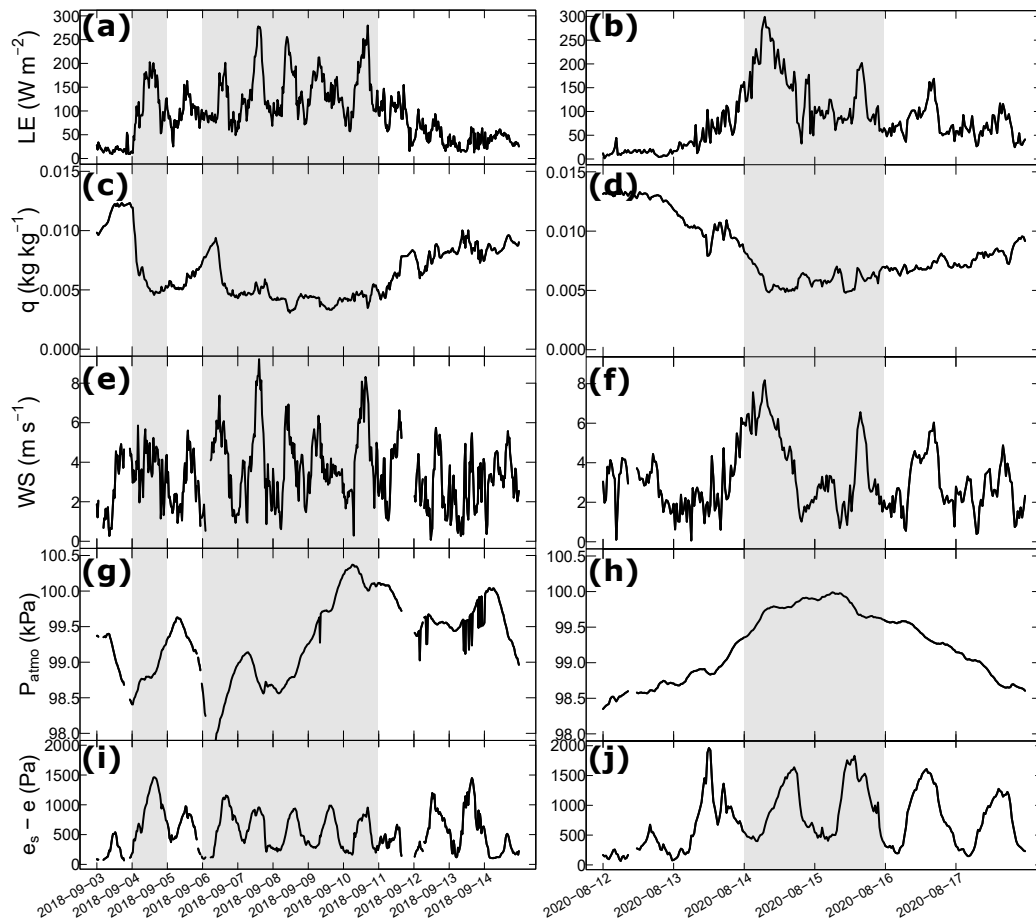
Accepted Article

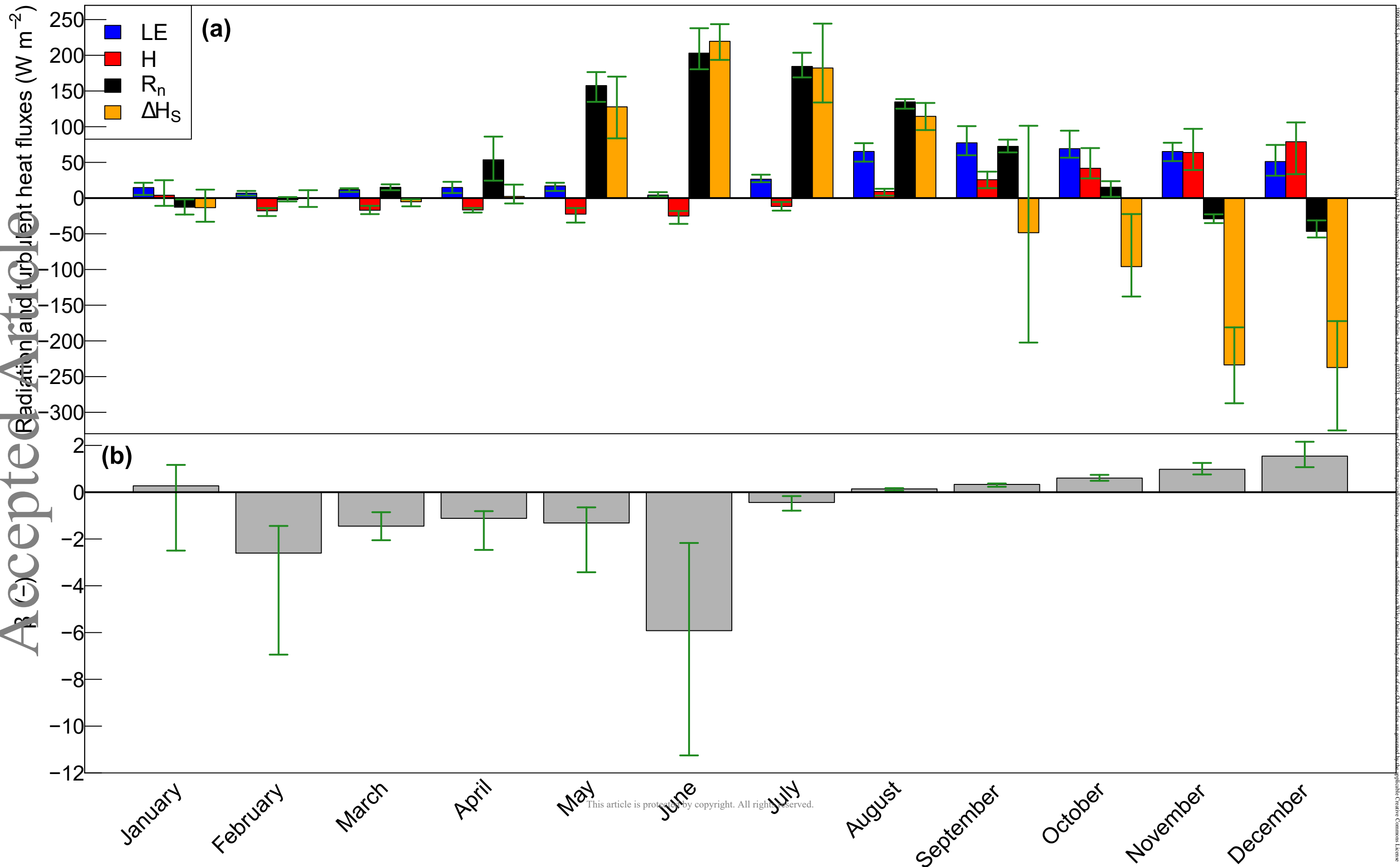


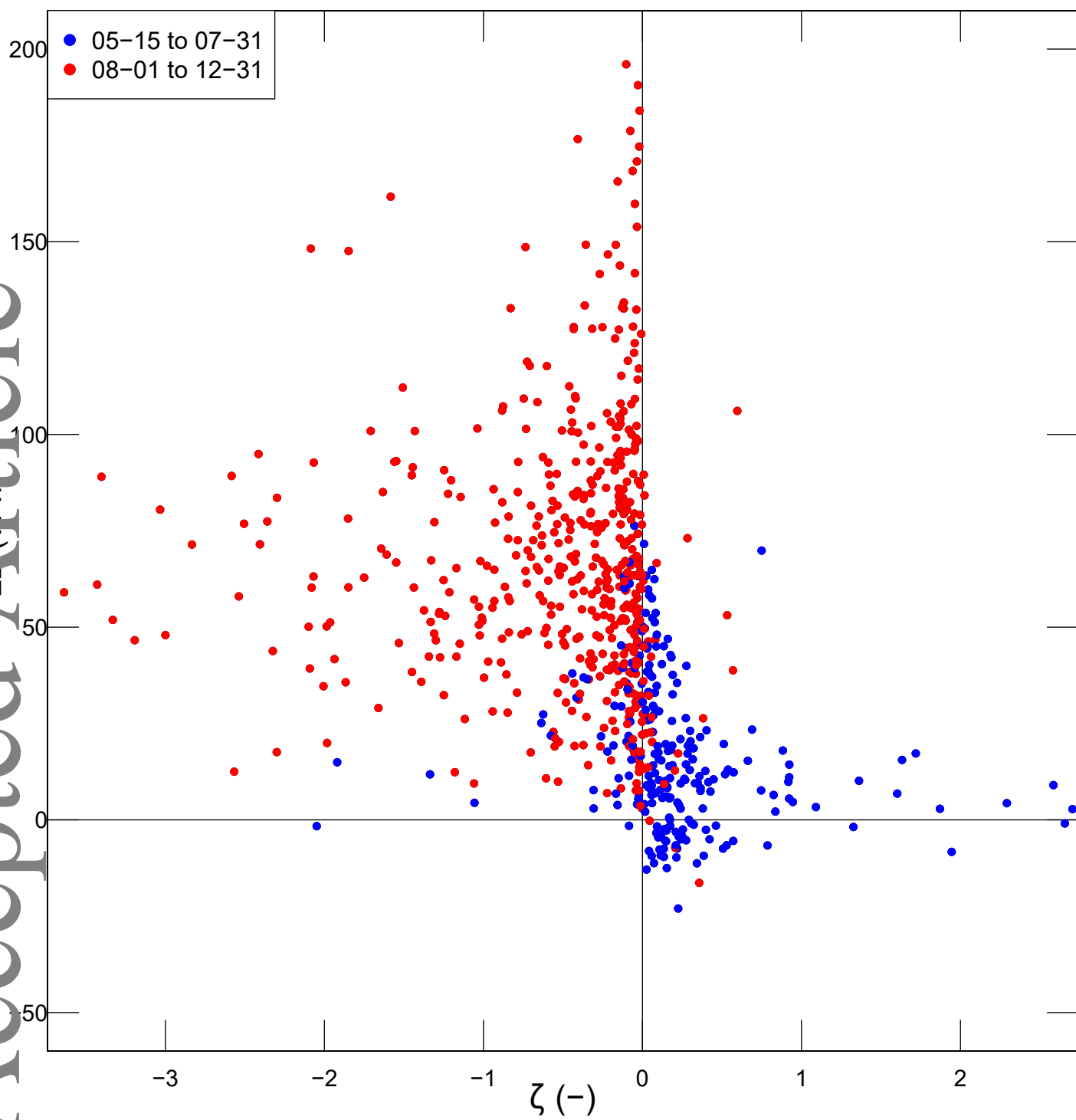
This article is protected by copyright. All rights reserved.

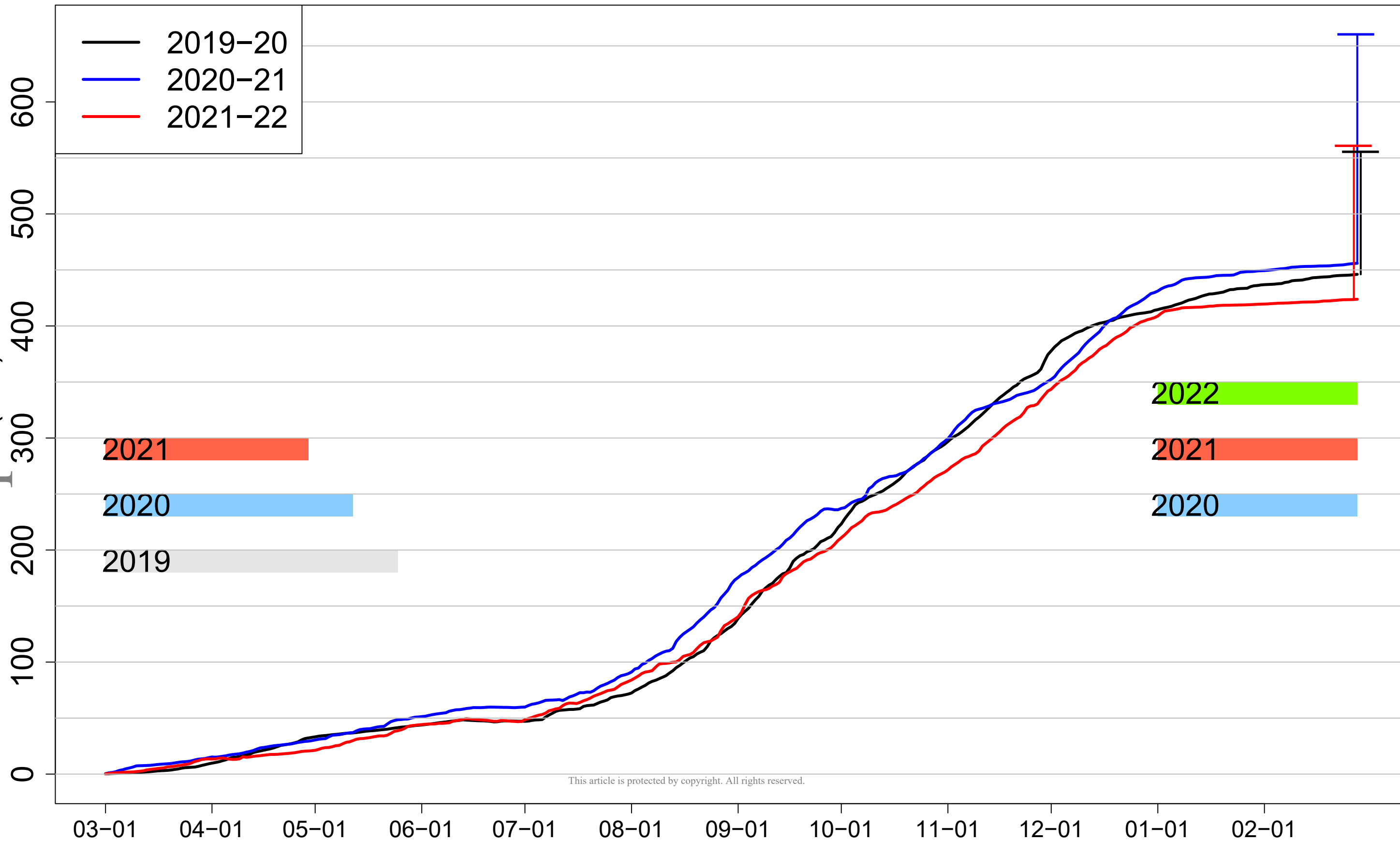


This article is protected by copyright. All rights reserved.









This article is protected by copyright. All rights reserved.

250

200

150

100

50

0

2019
2020
2021

Jan

Feb

Mar

Apr

May

Jun

Ju

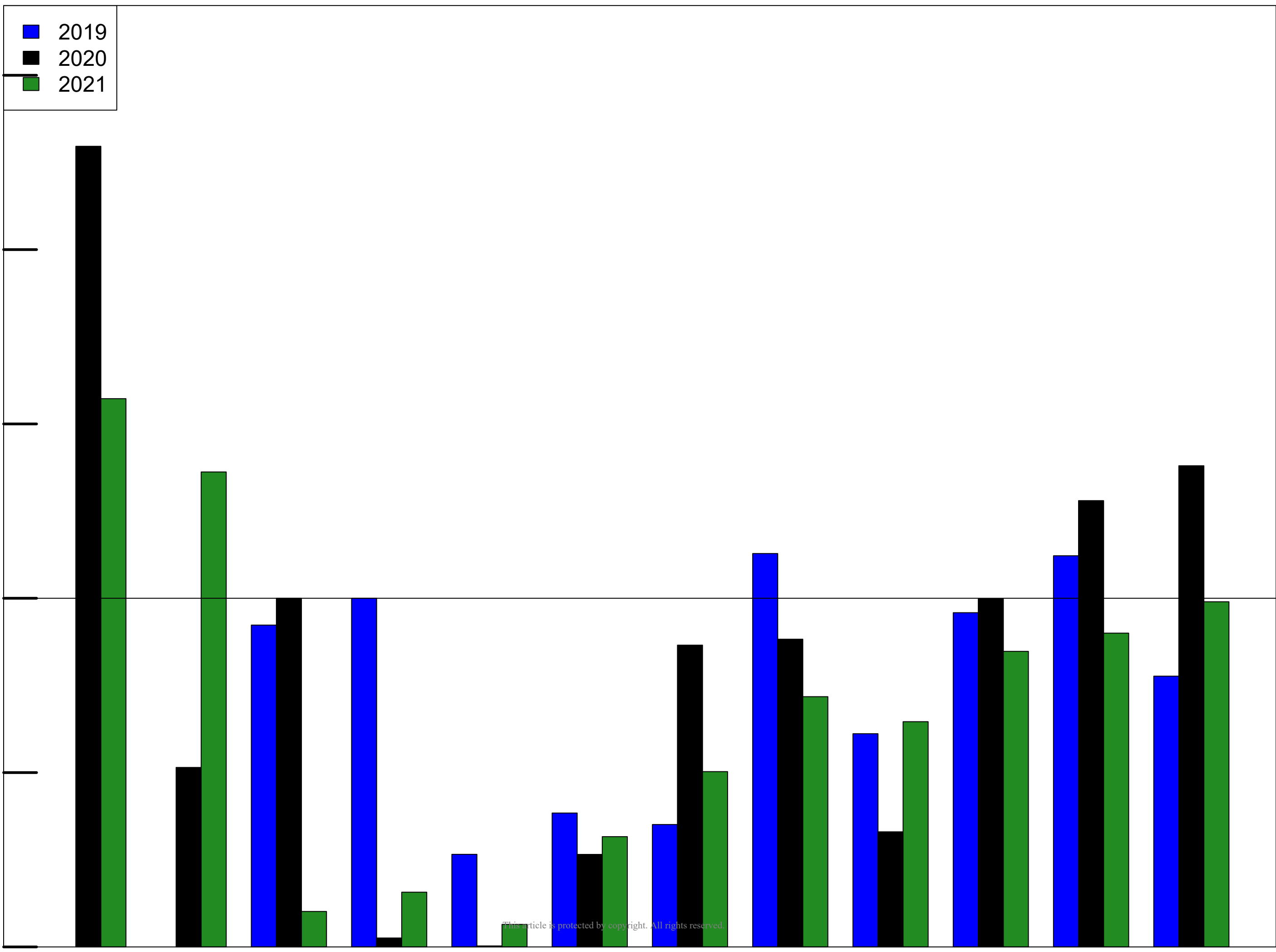
Aug

Sep

Oct

Nov

Dec



This article is protected by copyright. All rights reserved.